REPORT DOCUMENTATION PAGE

Form Approved OMB NO. 0704-0188

1. REPORT DATE (DD-MM-YYYY)	2. REPORT TYPE	3. DATES COVERED (From - To)
04-10-2013	Final Report	1-Oct-2012 - 30-Jun-2013

4. TITLE AND SUBTITLE

Mechanics of Multiscale Energy Dissipation in Topologically Interlocked Materials-11.1 STIR

5a. CONTRACT NUMBER

W911NF-12-1-0370

5b. GRANT NUMBER

5c. PROGRAM ELEMENT NUMBER

611102

6. AUTHORS

Thomas Siegmund

5d. PROJECT NUMBER

5e. TASK NUMBER

5f. WORK UNIT NUMBER

7. PERFORMING ORGANIZATION NAMES AND ADDRESSES

Purdue University
Sponosored Program Services
155 S Grant Street
West Lafayette, IN   47907   -2114

8. PERFORMING ORGANIZATION REPORT NUMBER

9. SPONSORING/MONITORING AGENCY NAME(S) AND ADDRESS(ES)

U.S. Army Research Office
P.O. Box 12211
Research Triangle Park, NC 27709-2211

10. SPONSOR/MONITOR'S ACRONYM(S)

ARO

11. SPONSOR/MONITOR'S REPORT NUMBER(S)

62552-EG-II.3

12. DISTRIBUTION AVAILIBILITY STATEMENT

Approved for Public Release; Distribution Unlimited

13. SUPPLEMENTARY NOTES

The views, opinions and/or findings contained in this report are those of the author(s) and should not contrued as an official Department of the Army position, policy or decision, unless so designated by other documentation.

14. ABSTRACT

The objective of the present study is to provide understanding of potential energy absorption and dissipation mechanisms and benefits of topologically interlocked material assemblies (TIMs) under impact loading. The study is motivated by earlier findings that TIMs under low rate loading demonstrated attractive properties including the capability to arrest and localize cracks and to exhibit a quasi-ductile response even when the unit elements are made of brittle materials. It is hypothesized that TIMs due to their modularity would possess advantageous impact

15. SUBJECT TERMS

16. SECURITY CLASSIFICATION OF:			17. LIMITATION OF ABSTRACT	15. NUMBER OF PAGES	19a. NAME OF RESPONSIBLE PERSON
a. REPORT	b. ABSTRACT	c. THIS PAGE			Thomas Siegmund
UU	UU	UU	UU		19b. TELEPHONE NUMBER
					765-494-9766

Report Title

ABSTRACT

The objective of the present study is to provide understanding of potential energy absorption and dissipation mechanisms and benefits of topologically interlocked material assemblies (TIMs) under impact loading. The study is motivated by earlier findings that TIMs under low rate loading demonstrated attractive properties including the capability to arrest and localize cracks and to exhibit a quasi-ductile response even when the unit elements are made of brittle materials. It is hypothesized that TIMs due to their modularity would possess advantageous impact characteristics. In order to test this hypothesis, a series of computational experiments on the dynamic loading of TIMsare conducted. Results obtained in this study are presented for a planar TIM configuration based on a dense packing of tetrahedral unit elements to form an energy absorption layer. Finite element models are calibrated on samples fabricated using fused deposition (FD) additive manufacturing (AM).Employing the Lambert-Jonas formula to interpret the numerical data, it is demonstrated that TIMs can absorb more impact energythan conventional solid plates. An extended two-stage Lambert-Jonas model is defined such that accurate description of the impact response of TIMs is obtained. We demonstrate a method for integrated CAD-CAM-3D AM and FE analysis.

Enter List of papers submitted or published that acknowledge ARO support from the start of the project to the date of this printing. List the papers, including journal references, in the following categories:

(a) Papers published in peer-reviewed journals (N/A for none)

Received   Paper

TOTAL:

Number of Papers published in peer-reviewed journals:

(b) Papers published in non-peer-reviewed journals (N/A for none)

Received   Paper

TOTAL:

Number of Papers published in non peer-reviewed journals:

(c) Presentations

Y.-Z. Feng, E. Habtour, J. Riddick, T. Siegmund, "Damage analysis of a hybrid energy absorption layer based on the principle of topologically interlocking materials," Proceedings of the 2013 International Mechanical Engineering Congress and Exposition, The American Society of Mechanical Engineers. San Diego, CA, Nov. 2013.

Y.-Z. Feng, T. Siegmund, "Dynamic and failure analysis of topologically interlocked materials subjected to impact," EMI-2013, 2013 Engineering Mechanics Institute Conference of ASCE, August 4-7, 2013, Northwestern University, Evanston, IL, USA, Abstract #371.

Number of Presentations: 2.00

<div align="center">

Non Peer-Reviewed Conference Proceeding publications (other than abstracts):

</div>

<u>Received</u>   <u>Paper</u>

   TOTAL:

Number of Non Peer-Reviewed Conference Proceeding publications (other than abstracts):

<div align="center">

Peer-Reviewed Conference Proceeding publications (other than abstracts):

</div>

<u>Received</u>   <u>Paper</u>

   TOTAL:

Number of Peer-Reviewed Conference Proceeding publications (other than abstracts):

<div align="center">

(d) Manuscripts

</div>

<u>Received</u>   <u>Paper</u>

09/30/2013   2.00   Yuezhong Feng, Thomas Siegmund, Ed Habtour, Jaret Riddick. Impact Mechanics of Topologically
                     Interlocked Material Assemblies,
                     IN submission (11 2013)

   TOTAL: **1**

Number of Manuscripts:

<div align="center">

Books

</div>

TOTAL:

Patents Submitted

Patents Awarded

Awards

Graduate Students

NAME	PERCENT_SUPPORTED
FTE Equivalent:	
Total Number:	

Names of Post Doctorates

NAME	PERCENT_SUPPORTED
Yuezhong Feng	1.00
FTE Equivalent:	**1.00**
Total Number:	**1**

Names of Faculty Supported

NAME	PERCENT_SUPPORTED	National Academy Member
Thomas Siegmund	0.05	
FTE Equivalent:	**0.05**	
Total Number:	**1**	

Names of Under Graduate students supported

NAME	PERCENT_SUPPORTED
FTE Equivalent:	
Total Number:	

Student Metrics
This section only applies to graduating undergraduates supported by this agreement in this reporting period

The number of undergraduates funded by this agreement who graduated during this period: 0.00

The number of undergraduates funded by this agreement who graduated during this period with a degree in science, mathematics, engineering, or technology fields:...... 0.00

The number of undergraduates funded by your agreement who graduated during this period and will continue to pursue a graduate or Ph.D. degree in science, mathematics, engineering, or technology fields:...... 0.00

Number of graduating undergraduates who achieved a 3.5 GPA to 4.0 (4.0 max scale): 0.00

Number of graduating undergraduates funded by a DoD funded Center of Excellence grant for Education, Research and Engineering: 0.00

The number of undergraduates funded by your agreement who graduated during this period and intend to work for the Department of Defense 0.00

The number of undergraduates funded by your agreement who graduated during this period and will receive scholarships or fellowships for further studies in science, mathematics, engineering or technology fields: 0.00

Names of Personnel receiving masters degrees

NAME

Total Number:

Names of personnel receiving PHDs

NAME

Total Number:

Names of other research staff

NAME   PERCENT_SUPPORTED

FTE Equivalent:
Total Number:

Sub Contractors (DD882)

Inventions (DD882)

Scientific Progress

Our research under this award has focussed on the impact mechanics of topologically interlocked materials. In the past these material systems have only be studies under quasi-static loading. Topologically interlocked materials are assemblies of platonic solid shaped unit elements. These structures transfer loads under transverse loading, limit damage to the unit element in which damage occurs and allow for a bottom-up structure design.

We have accomplished the following milestones:
(1) Developed an integrated CAD-3DAM-FEM approach. The integration of all these individual components of a CAE approach to the analysis of material and structures is enabled by the use of the Python programming language.
(2) Developed a method for a rational approach to parameter calibration in TIM model systems. We have defined this approach to determine the contact stiffness between unit elements as well as the friction conditions. Excellent agreement between model and simulation is obtained.
(3) Provided understanding of the high rate loading (constant rate) of TIM assemblies. We have found that the principle underlying mechanism of the formation of force chains is again present, albeit somewhat mitigated if slip is considered. High rate loading response emerges as the linear superposition of the initial inertia response of the TIM and the subsequent quasi static TIM response (which is characterized by a force deflection response of perfect damageable character).
(4) Provide understanding of the impact response. Impact response of TIMs again is characterized by the formation of force chains. We find that the residual velocity characteristics can be described by the Lambert-Jonas equations. Still, in more detail we observe that in that response at least two characteristic domains emerge, each of which can be characterized by its own LJ response. At low velocities, a strong interaction between penetrator and target is present, while for the high velocity domain no such interaction exist.
(5) Investigate the influence of local material failure on TIM failure. We embed cohesive zone models for the description of material failure into the analysis. We find that residual velocities are potentially favorably affected by fragmentation. We also determine a size effect on the predicted residual velocities. TIM systems response is found to be dependent on the material internal length scale as introduced by the cohesive zone model.

Technology Transfer

Mechanics of Multiscale Energy Dissipation in Topologically Interlocked Materials-11.1 STIR

Final Report

PI: T. Siegmund

School of Mechanical Engineering

Purdue University

West Lafayette, IN 47907

September 2013

1. Introduction

In the design of multifunctional structural components it is essential to go beyond the selection of materials with the appropriate properties. Developing logical and hybrid structures can be effective in solving some of critical and challenging engineering problems that may require multifunctionality without developing new and exotic material composition. Hybrid material systems are understood to provide efficient alternatives to conventional materials and fill holes in material property spaces [1-3]. One of the methods relevant for the creation of hybrid material systems is that of segmentation. Thereby, a hybrid material system is created from the bottom-up by the ordered assembly of unit elements. Hybrids created by this approach allow for the exploration of important material mechanics concepts such as topological toughening and of size effects. Past studies on hybrid materials created by assembly have predominately considered quasi-static loading conditions. The aim of the present study is to explore the response of such material systems to high rate loading and to impact. In particular, the study is concerned with one class of segmented hybrids, Topologically Interlocked Material assemblies, TIMs. In a TIM system, each individual unit element is topologically confined by its neighbors due to the oblique angles of the basic unit elements; therefore no binders are necessary to maintain the integrity of the assembly [4-8]. We hypothesize that the topological interlocking of the unit (or fragment) elements would provide for an enhancement in the impact resistance compared to monolithic solids.

The concept of topological interlocking assemblies has attracted some interest in the recent past. Proposed by Glickman [8] with the name of G-Block for the reduction of sub-structure and diminished maintenance cost for paving system, expanded, generalized and termed with the current name by Dyskin et al. [4, 9, 10], TIMs can be considered as novel mechanical meta-materials as these derive their unique properties not from composition but structure. Forces and energy can only be transmitted through the contact surfaces; accordingly, there are no tensile forces developed when TIMs carry loads. These unique characteristics of TIMs provide unique properties that can be utilize to create adaptive and configurable structures to harsh conditions such as random and harmonic vibrations, thermal loads, repetitive shocks and acoustic attenuation. For example, Dyskin et al. [4, 5, 7, 9, 10] introduced the general concept of TIM, and demonstrated the requirements for basic elements to assemble a TIM tile. Estrin et al . [11] assembled TIMs with identical cubes and tested their responses with point load tests. Schaare et al. [12] investigated the response of cube-based TIMs to point loading both experimentally and numerically. Brugger et al. [13] conducted indention experiments on TIMs assembled by osteomorphic ice blocks and plaster made cubes. Their results showed that TIM composed of cube elements can experience negtive stiffness when unloading. Dyskin et al. [14] revealed that TIMs are damage tolerant in that cracks inside of one unit

element will not propagate across the contact interface into adjacent units. Khandelwal et al. [15] experimentally examined the quasi-static responses of TIMs asembled with regular tetrahedra, and proposed an analytic model to predicted the quasi-static beaviors of TIM with thrust line theory. Mather et al. [16] studied the remanufacturability of TIMs, illustrated that only small portion of units could not be reused after failure of the TIMs. And for applications of TIMs, Estrin et al. [17] proposed the potential application of TIM as protective tiles for the space shuttle. Carlesso et al. [18] illustrated TIM composed by porous osteomorphic blocks enhances sound absorption because of the gaps among basic blocks.

The present investigation is aimed at understanding the response mechanism of TIMs due to impact loading, and the investigation of potential benefits of TIMS in energy absorption, as well as mechanical and structural applications. TIMs consists of dense packing of tetrahedral unit elements made of Acrylonitrile Butadiene Styrene (ABS) material, which were fabricated using fused deposition modeling (FDM) additive manufacturing (AM) motivate the material system under investigation [15]. Limited exploratory research has been done in understanding the mechanical characteristics of these novel structures, more specifically TIMs subject to low velocity impact. Plates subjected to impact are of great research interest for protection purpose, and extensive work has been reported on different types of systems subjected to ballistic impact [19-27]. Most recently, Wadley et al. [28] studied sandwich structures with different shapes of core material under ballistic impact. Their results demonstrate that sandwich structure performance can be improved with topological optimization of core materials. In the present study, the impact velocities considered are much lower than the dilatational wave speed of the material in the unit elements ($V_{imp} < c_d/10$). The finite element method was employed to conduct numerical experiments. First, the model is calibrated on experimental data of low and constant velocity loading. Then, the response under constant applied velocity is considered, and the contributions of inertia, elastic resistance, and contact and friction to the mechanical resistance are explored. Subsequently, impact loading is considered and the formulations of Recht and Ipson [29] as well as Lambert and Jonas [30] are employed to characterize the velocity response. These models are reformulated to provide specific insight into the impact response of the TIM assemblies. A comparison to typical data on monolithic structures under impact is made.

2.　Python Scripting Based Model Creation and Manufacturing

The ABAQUS Scripting Interface enables the user to effectively customize the creation of finite element models. With the API, one can automate repetitive tasks, extend functionality and enhance the interface through the use of Python. What makes this scripting language so powerful is the fact that for every feature in `ABAQUS/CAE`, there is a corresponding Python

script command that can be modified to provide greater functionality and more effective automation. In the present project, Python scripts were used to create `ABAQUS/CAE` models, define material properties, generate meshing, apply boundary conditions and loads, and to submit job for analysis. Furthermore, the Python scripts were also employed to generate CAD models for additive manufacturing. Granular crystals are considered as assemblies of many identical unit elements. Therefore, many repetitions in the model creation would be needed if the process was conducted without a script. The granular crystal considered here was an assembly of interlocking tetrahedra arranged in a dense packing in the plane [31]. The granular crystal – also called a Topologically Interlocking Material (TIM) [10] - is confined at its boundaries by rigid abutments, and a projectile type loading is applied at the center of the assembly via a rigid body (see Figure 1).
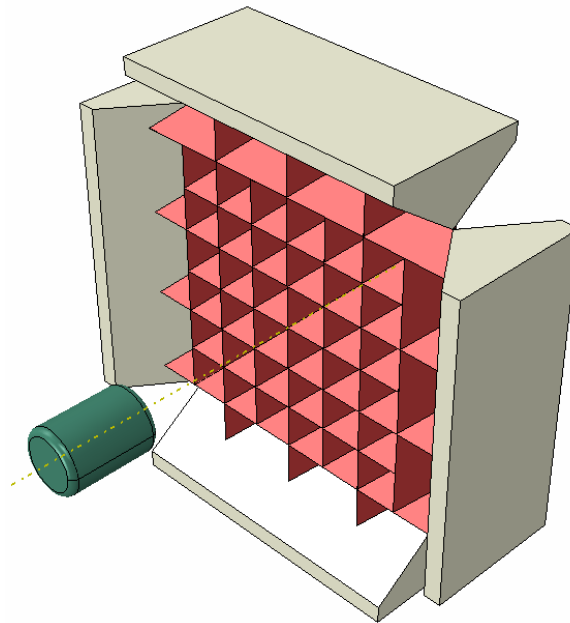
Figure 1. CAD model of the TIM plate and the projectile

The general procedure for generating simulation with Python script is as follows:

(1). Create a model database named as *tetrahedron*

(2). Create a part named as *tet*, which is an individual tetrahedron element of the TIM plate. Define the material properties for the tetrahedron and assign them to the part of *tet*. Set seeds, mesh the tetrahedron part, assemble the part, pattern the instance and position them by translation and rotation.

(3). Create a part named as *boundary*, which is one side of the support frame. Define the material properties and assign them to the part of *boundary*. Set seeds, mesh the frame part, assemble the part, pattern the instance and position them by translation and rotation.

(4). Create a part named as *indenter*, which is used to impact the TIM plate. Define the material properties and assign them to the part of *indenter*. Set seeds, mesh the tetrahedron part, assemble the part, and position it by translation and rotation.

(5). Define the contact interactions and rigid bodies. In the simulation, the indenter/projectile and the support frame are considered as rigid bodies.

(6). Apply boundary conditions and loads. For the support frame, all degrees of freedom are constrained. A predefined velocity is applied on the projectile, which will impact the TIM plate at the plate center.

(7). Submit the job for analysis.

Parameterization is a distinct advantage of Python scripting for ABAQUS as it allows for high efficiency in modeling, particularly for dimensional analysis. For example, Figure 2 shows a TIM tile with 7×7 tetrahedra. To have a TIM tile with 10×10 tetrahedra (Figure 3), we just need to set the number of tetrahedral in one row/column to be 10.
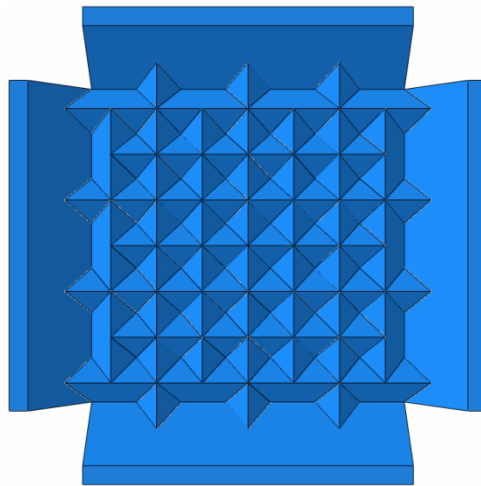

Figure 2: TIM plate with 7×7tetrahedra

Two basic dimensions for the TIM plate are the edge length of individual tetrahedron and the numbers of tetrahedra in one row/column. Therefore these two variables are defined as the basic dimensional parameters for the analysis in the Python scripts and all other dimensions can be obtained based on them. All the material properties are also parameterized, which means that the material properties can be changed very easily.
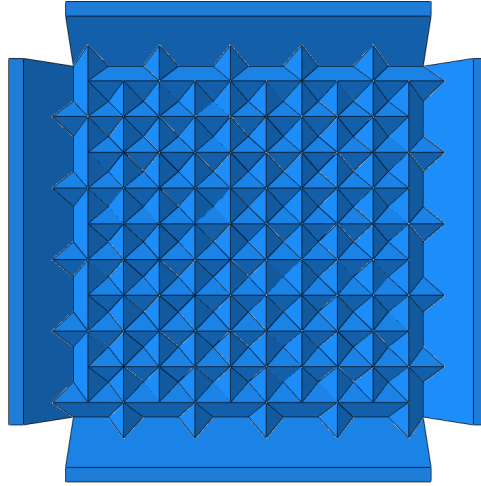
Figure 3: TIM plate with 10×10 tetrahedra

Cracks may initiate and propagate in materials when they are subjected severe loading conditions. Many approaches have been developed to predict the process of crack initiation and propagation in the frame of fracture mechanics [32, 33]. Abaqus has implemented cohesive zone method (CZM), virtual crack closure technique (VCCT), and extended finite element method (XFEM) to simulate the crack propagation. With the current release of Abaqus package (Abaqus 6.12), all the three methods can work under Abaqus/standard, while only the CZM can be used under Abaqus/explicit. Therefore CZM is employed for the current project to predict the damage of topologically interlocked material (TIM) subjected to impact. Moreover, the microstructure nature of the tetrahedra to assemble the TIM tile, which are manufactured by 3D printing, is very desirable to the CZM.

On the other hand, the creation of CZM may be very tedious if possible, particularly when the models are complex, since the modification of nodal coordinates is necessary to have zero thickness cohesive layers. With its powerful loop, condition and selection statements, Python scripting can dramatically improve the efficiency of modeling CZ with Abaqus. Furthermore, with the help of parameterization, it is very convenient to modify the number of CZ layers in a tetrahedron, or even the orientation of the CZ layer.

The additional steps for CZ enhanced model are to define the CZ properties and create cohesive elements, comparing with the models without cohesive connections. In the simulations, the bilinear traction-separation law is used to describe the CZ constitutive behavior. In choosing the CZ properties, such as failure displacement, stiffness and softening, both prediction accuracy and computational resources need to take into consideration [34].

Figure 4 illustrates the procedure of creating the cohesive elements in a tetrahedron part. First, layered tetrahedron part is created (Figure 4a) and meshed (Figure 4b). To have zero thickness cohesive zones, the cohesive element nodes are modified (Figure 4c).

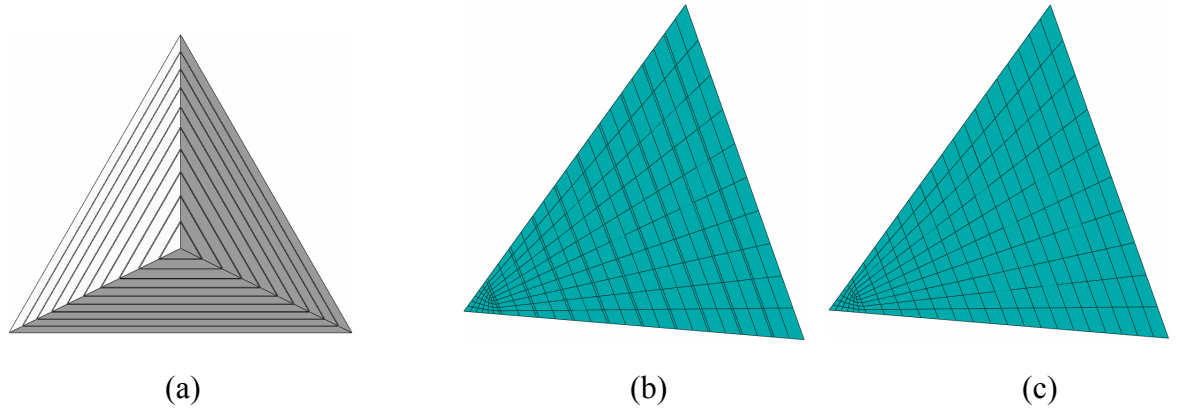(a)   (b)   (c)

Figure 4: Cohesive zone model of tetrahedron

(a) Geometry model; (b) mesh without modification; (c) mesh with modification

Python scripts can also be applied to the creation of CAD model and STL files for the 3D print manufacturing of granular crystals. In this application the Python script creates ACIS SAT 3D model files (.sat), which then further are saved in the STL file format for processing with 3D printers such as the Objet Connex 350 (Stratasys). Figure 5 shows the CAD model for the TIM plate with 7×7 tetrahedra. Figure 6 shows the importation to CAD software of the CAD model created by the Python scripts. Figure 7 a screen shot of the printing machine interface software, and Figure 8 the final 3D printed prototype.
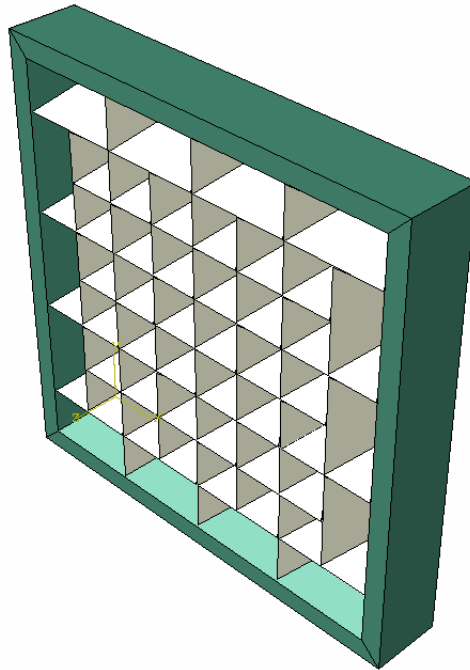

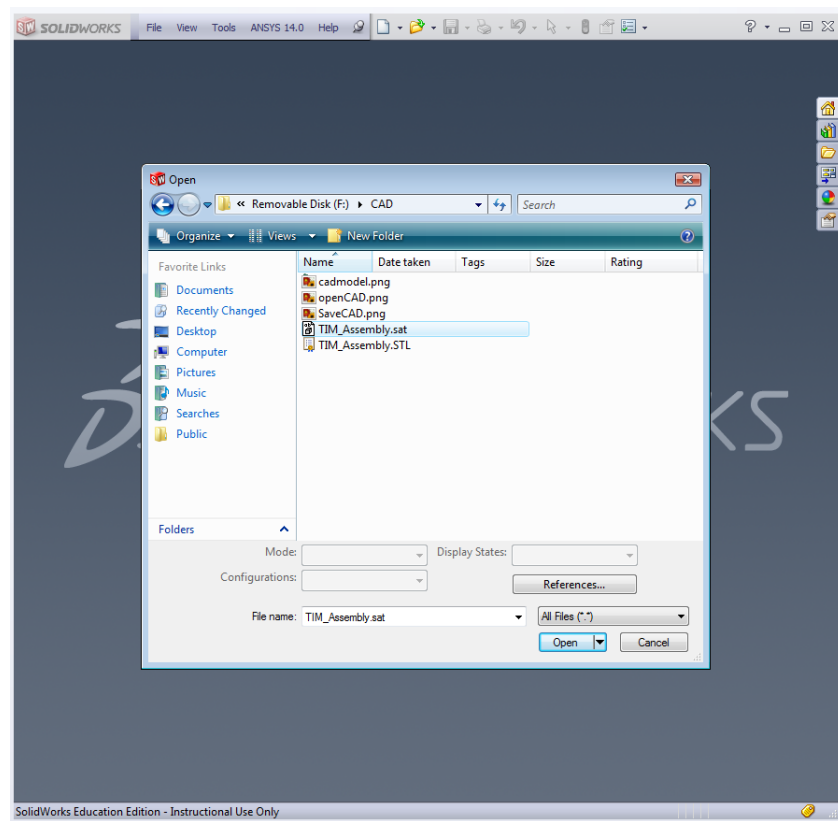Figure 5: CAD model for the TIM plate with 7×7 tetrahedra

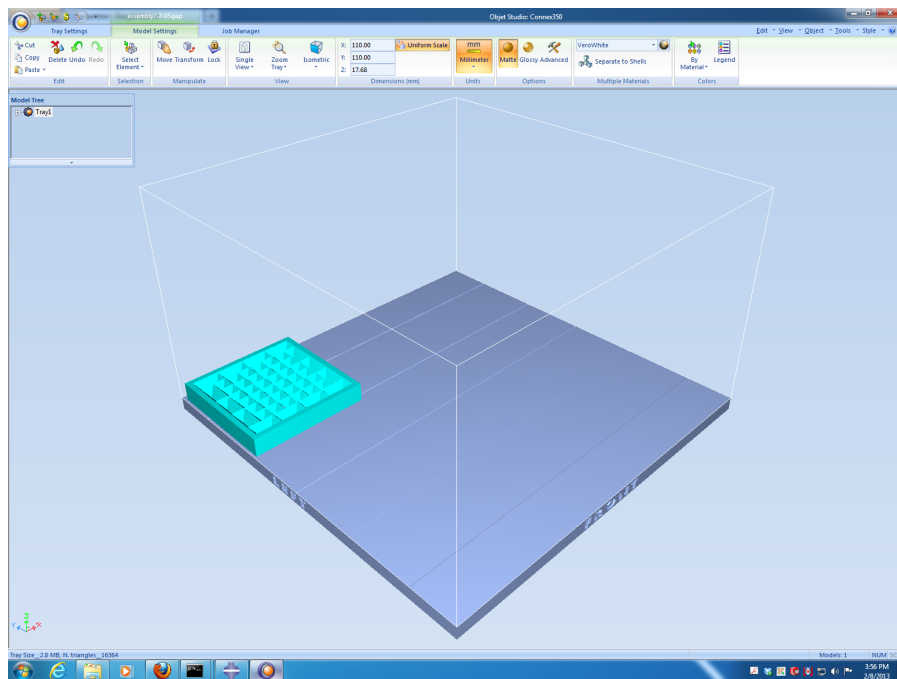Figure 6: Importing the CAD file to CAD software

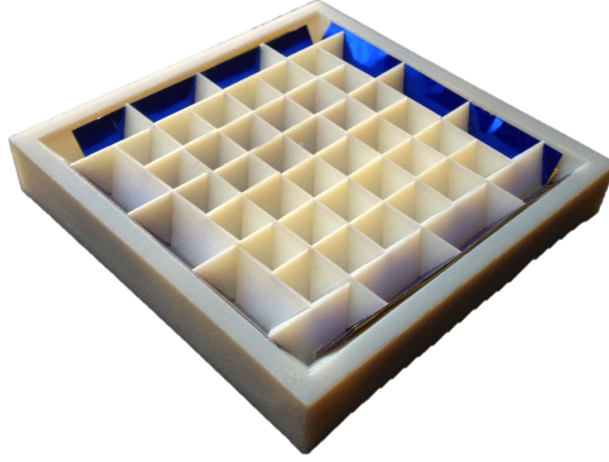Figure 7: Printing the CAD model with printing machine interface software

Figure 8: 3D printed prototype of a TIM plate with 7×7tetrahedra

3. FEM Model Definition and Calibration

3.1. Model Definition

Figure 9 shows the model system under consideration with (a) a regular tetrahedron as the basic unit of the TIM assembly, (b) a boundary element (termed abutment), (c) the indenter/projectile and the center five tetrahedra onto which the indenter transfers the load, (d) the TIM tile composed with identical regular tetrahedra, (e) the overall TIM assembly together with the cylinder shaped indenter/projectile. In the model assembly, total of $N×N$=49 identical tetrahedra are assembled in a square lattice pattern into a monolayer TIM assembly [4, 8, 15],and confined with abutments along the edges of the assembly. The edge length of an individual regular tetrahedron is s_0. The other dimensions of the TIM assembly can be derived as the thickness of the monolayer$t = s_0/√2$, the dimension of the mid-plane of the TIM assembly,$L=s_0×(N/2)$. Here, the TIM assembly is characterized by $N = 7$ and$s_0 = 25$ mm, such that $t = 17.7$ mm and$L = 87.5$ mm.
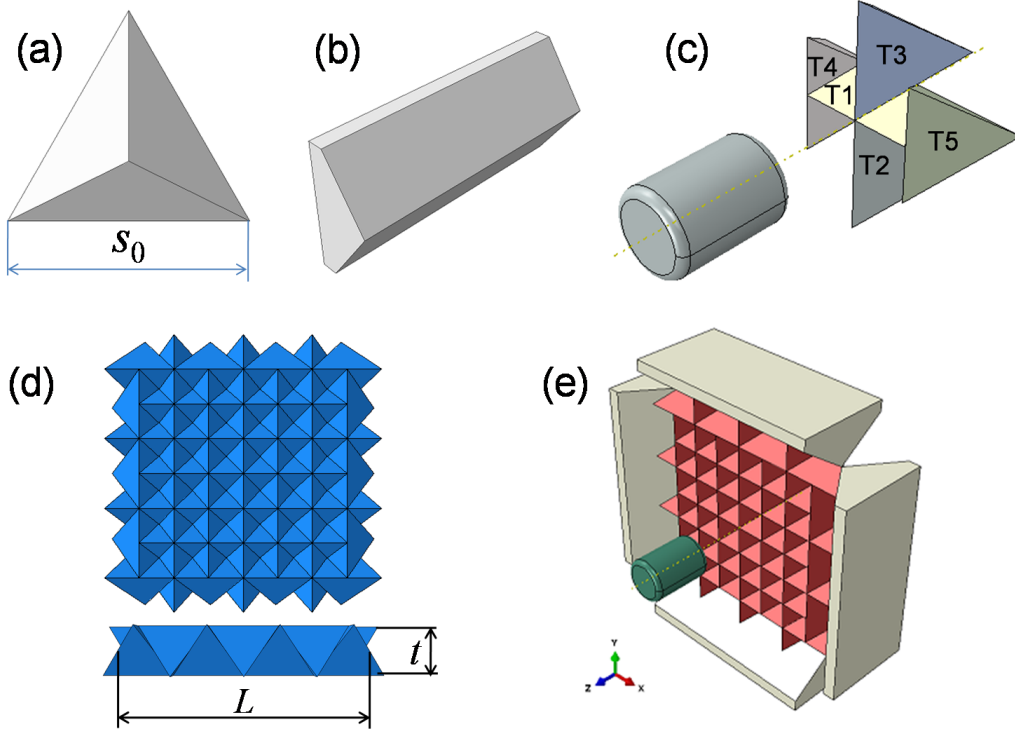
Figure 9. Model of Topologically Interlocked Material (TIM) assembly: (a) Unit element regular tetrahedron, (b) Abutment (c) Indenter/projectile and center tetrahedra, (d) TIM tile, (e) Overall assembly.

Two loading conditions were considered: (1) constant velocity loading by an indenter, and (2) impact loading by a projectile. In both cases the load was applied to the center of the TIM assembly such that the indenter/projectile interacts directly with tetrahedra #1, #2, and #3 of the assembly. The diameter D of the indenter/projectile is $D = L/5$.

Tetrahedra were considered to be isotropic and elastic. Motivated by prior experiments on TIM assemblies in [15], the material properties of ABS were employed (Young's modulus E=1.827 GPa, Poisson's ratio $\nu = 0.35$, density $\rho_0 = 950$ kg/m^3). One tetrahedron thus possesses a mass of m_0=1.75×10^{-3} kg and the overall assembly weighs 8.58×10^{-2} kg. The abutments as well as the indenter/projectile were considered as rigid bodies. The density of the projectile was $\hat{\rho}$ =1470 kg/m^3. The contact properties, i.e., the contact pressure-overclosure relation and the friction condition were not directly available. A Coulomb friction model was employed which introduces the coefficient of friction μ. For the normal contact behavior, it was assumed that contact pressure p_c is linearly dependent on the overclosure Δ_n as $pc = K_c\Delta_n$, where $K_c = (K^*E^*)/(\pi s_0)$ is the contact stiffness with K^* a normalized contact stiffness, and $E^* = E/[2(1-\nu^2)]$. This type of interactions was adopted to

describe the contact behaviors for the inter-tetrahedra, tetrahedron-abutment and tetrahedra-indenter contacts. Experimental data on the low velocity impact response of TIM assemblies presented in [15] was used to calibrate the model parameters μ and K^*.

In the constant velocity cases, a predetermined displacement is applied on the indenter and the time interval of loading is varied in order to achieve a constant velocity V_0. In the impact cases, a projectile of a defined mass M with initial velocities V_{imp} strikes the TIM assembly. The mass of the projectile is chosen as 10% of the total mass of the 7×7 tetrahedra. The abutments are fixed in space in all cases.

Finite element models of the TIM assembly were constructed in the general purpose finite element code `ABAQUS` (Version 6.12) [35]. The finite element mesh employs, 3D linear solid element (`C3D8R` in the `ABAQUS` code) with each tetrahedron is comprised of 500 elements such that the overall model consisted of 24,500 elements. The model was solved using the `ABAQUS/Explicit` solver, and the general contact algorithm implemented in the `ABAQUS` software was employed. In all the simulations, one analysis step was defined. The automatic time increment algorithm was employed and the global stable increment estimator was selected. The step time period for constant velocity loading varies dependent on loading velocities while for impact loading an analysis interval of 5 ms is considered in all the cases.

3.2. Parameter Calibration

In the experiments presented in [15], a drop mass of M_{drop}= 6.21 kg and drop height H_{drop}= 36.58 mm were employed. Since the drop mass significantly exceeds that of the TIM assembly, a near constant velocity loading condition (V_0 = 0.925 m/s) was achieved in the experiment. The data of the forces – deflection record were presented in [15], and this data was used to calibrate the parameters μ and K^*.

The computational study provided the force-deflection curves of TIM for contact stiffness (K^* = 0.5) and different coefficients of friction. Figure 10 shows predicted force-deflection curves from computations considering a range of values of μ ($0.1 < \mu < 1.0$). In these calculations the contact stiffness was K^* = 0.5. In all cases a force – deflection response typical of TIM assemblies was predicted [15]. The force initially increases with the deflection; a peak force value is reached, followed by gradual softening until the resistance of the TIM assembly vanishes. The resistance of the TIM assembly to the applied load was found to increase with an increase in μ. The predicted peak force increased from 48.5 N to 513.0 N when μ was changed from μ = 0.1 to 1.0. The results also indicate an increase of the deflection to final collapse of the TIM with an increase in μ. For the lowest value of μ considered (μ=0.1), the load carrying capacity of the TIM vanishes at a deflection of 22.0 mm but this limiting deflection more than doubles for cases considering higher values of μ. The next set of

computations considered a range of contact stiffness values and constant coefficient of friction. Figure 11 shows reaction the predicted force-deflection records for computations considering variations in contact stiffness ($0.1 < K^* < 1.0$). In these calculations $\mu = 0.3$ was considered. It is found that the magnitude of the predicted forces increases with increased contact stiffness. The peak force was found to increase from approximately 52.0 N to 513.0 N as K^* was increased from $K^* = 0.1$ to 1.0. However, the deflection to loss of load carrying capacity did not vary significantly, and for all the cases was about 35.0 mm.

The results of the parametric computations indicate that the coefficient of friction affects both the magnitude of the force and the deflection to final failure, while the contact stiffness plays a role only in the force magnitude. Therefore, the following calibration procedure was followed. First, the coefficient of friction was calibrated with respect to the experimental results of the deflection to final failure. Then, the contact stiffness is selected to provide a final force - deflection response which fits that of the experiments presented in [15]. The calibrated parameters are $\mu = 0.2$ and $K^* = 0.38$. Model predictions of the force – deflection response obtained using the best-fit parameters for μ and K^* together with the experimental data are shown in Figure 12, and a good quantitative agreement is found. The residual deformations of the TIM assemblies after indention are shown for the experiment in Figure 13(a) [15], and the model simulation in Figure 13(b). A good qualitative agreement is obtained.
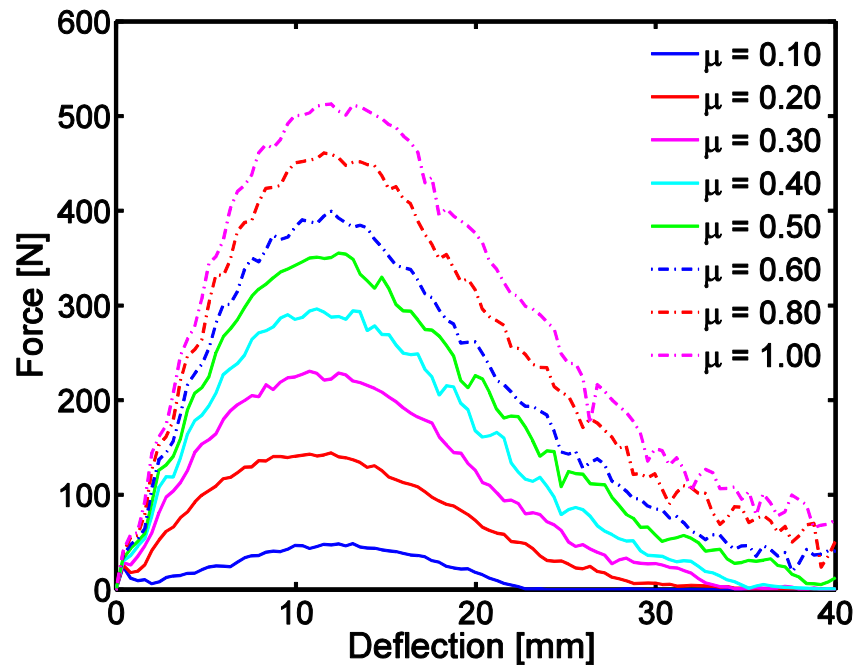

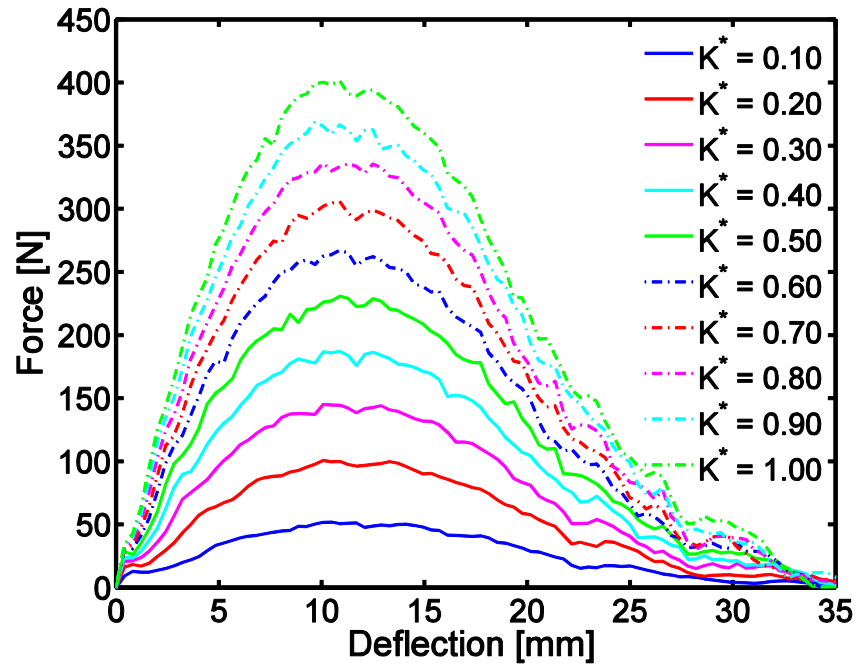Figure 10. Predicted force-deflection curves for a range of values of the coefficient of friction μ.

Figure 11. Predicted force-deflection curves for a range normalized contact stiffness values K^*.
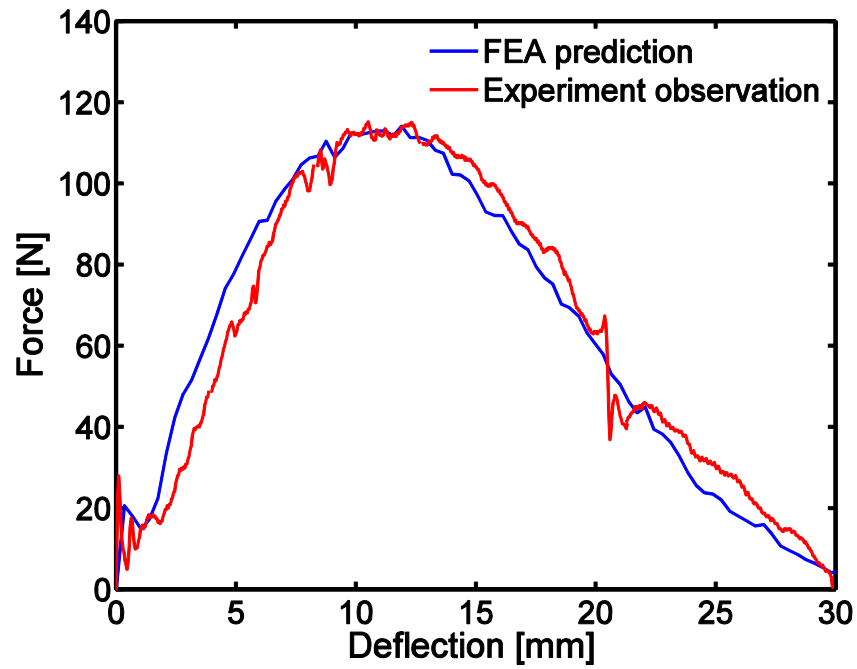

Figure 12. Force - deflection curves: experimental data [15] and best fit prediction.
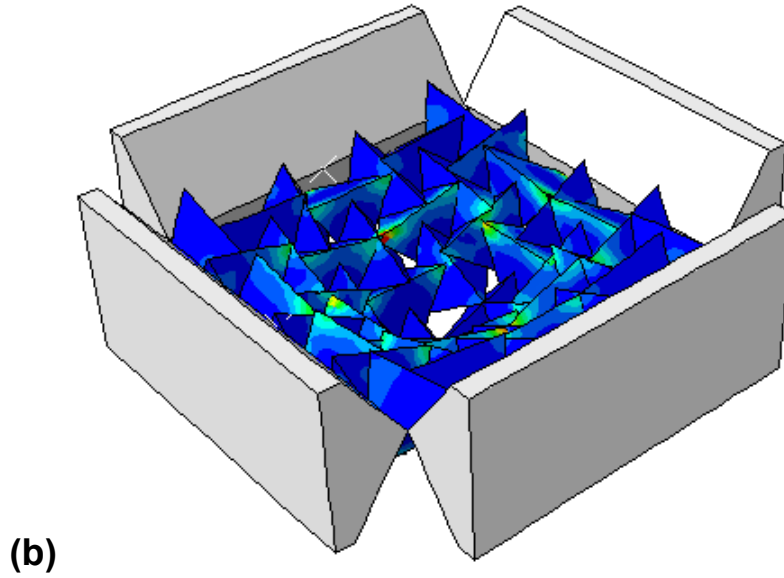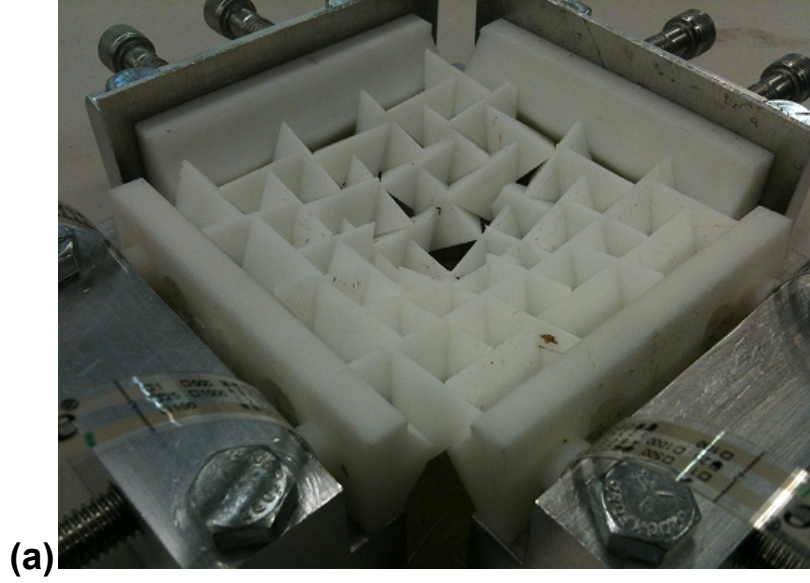
(a)

(b)

Figure 13. Deformed configurations of TIM assemblies after loading: (a) Experimental observation[15], (b) Model prediction with color contours depicting the residual stress state as characterized by the von Mises equivalent stress.

4. Dynamic Responses of TIM

4.1. Constant Velocity

Simulations of TIM subjected to constant velocity loading were conducted with applied velocities ranging from 0.1 m/s to 10 m/s. Figure 14 depicts the predicted force-deflection responses. For the lowest velocity case, V_0=0.1 m/s, the force increases smoothly with the increase of deflection, reaches its peak at a deflection of 11.0 mm then decreases gradually to zero. As the applied velocity increases, multiple peaks develop in the force-deflection curves. When the loading speed is greater than 1 m/s but less than 5 m/s, the first peak increases with

increasing velocity dramatically, while the second one maintains. When the loading speed is greater than 5 m/s, both peaks increase with increasing velocity.

Figure 15 shows the force-deflection relations for $V_0 = 0.1$ m/s with confinement, $V_0 = 4$ m/s with and without confinement, respectively. A simulation for unconfined TIM means the abutments, shown in Figure 9(d), are taken away in the computation. In this case, the force increase quickly to its peak then drops precipitously. There is no support force acting on the TIM tile, therefore, the force shown in the figure is due to the 'inertia' of the TIM tile. Since there is no such phenomenon occurred for the $V_0 = 0.1$ m/s case, the $V_0 = 0.1$ m/s case can be considered as quasistatic loading case. Therefore, as shown in Figure 15, the force-deflection curve for the $V_0 = 4$ m/s with confinement can be considered as the sum of the other two cases: quasi-static response and unconfined model with same impact velocity. Details of the determination of the inertia of TIM is discussed in Appendix.
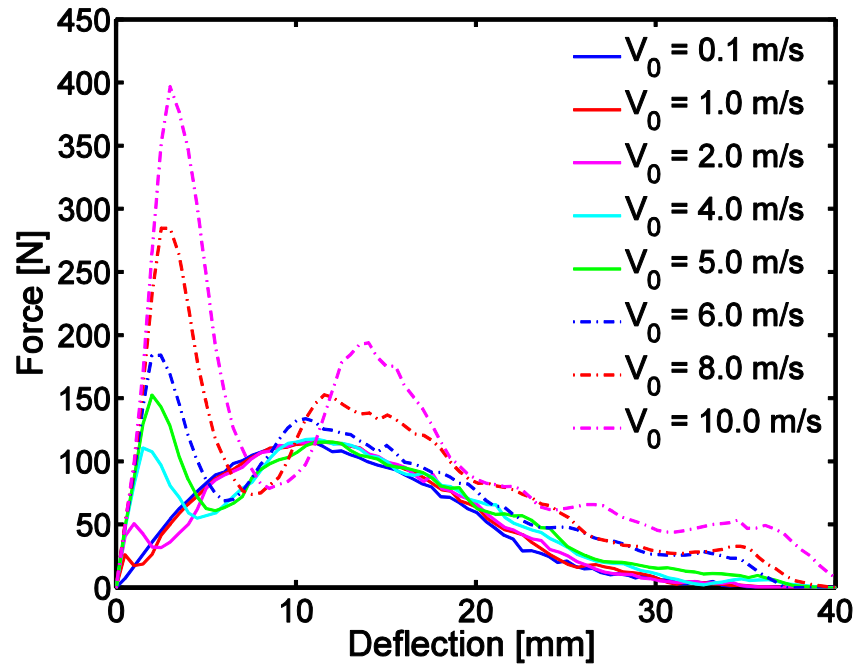

Figure 14. Predicted force - deflection curves for various constant velocities.
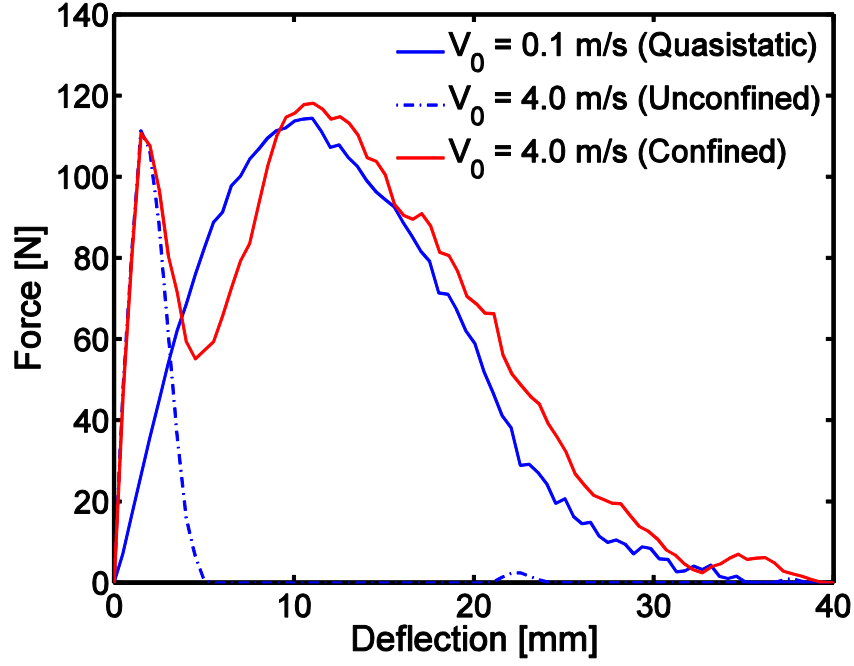
Figure 15. Predicted force - deflection curves for quasistatic loading with confined model, V_0= 4.0 m/s confined and unconfined models.

Figure 16 depicts the velocities of center tetrahedra during the indentation for relatively low and high indention speeds, V_0 = 4 and 10 m/s, respectively. The velocity of center tetrahedron is defined on the center of the center tetrahedron, and the center tetrahedron is the tetrahedron that the indenter directly strikes on, T1 as shown in Figure 9(c). The velocities increase with time at the beginning of indention, then decrease and increase alternatively, and finally they keep constant. Overshoots occur during indention. For V_0=10 m/s, after its peak value, the velocity of center tetrahedron drops far below the indentation speed because of the interaction with adjacent tetrahedra through contact. The indenter accelerates it again, which results in a second peak force in the force-deflection curves. For V_0=4 m/s, there also has time that the center tetrahedron speed is lower than that of indentation speed. However, the speed difference is not significant so the re-acceleration is not observed in the force-deflection curve.
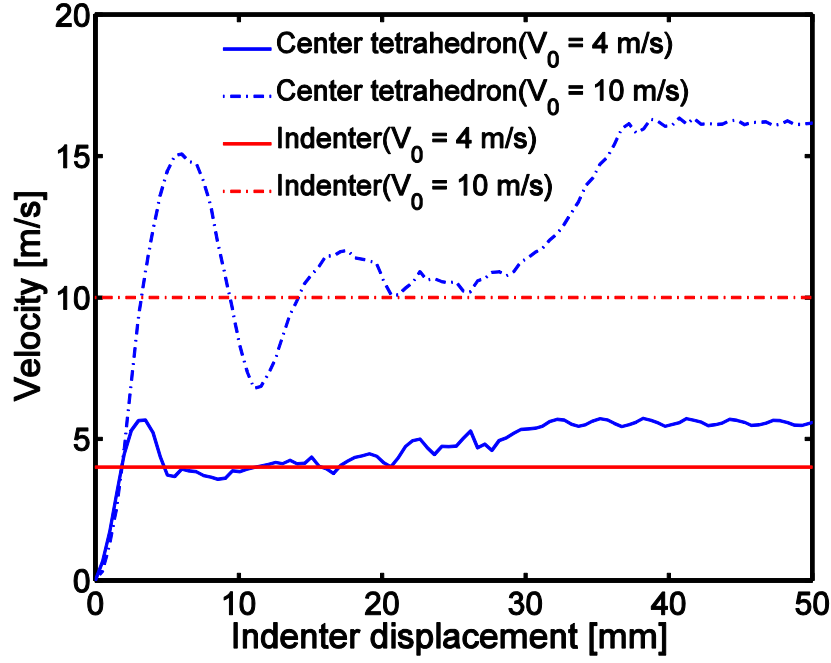
Figure 16. Predicted translational velocities (in load direction) of the center tetrahedron for loading speeds of V_0=4 m/s and 10 m/s.

4.2. Impact

All series of computations with impact velocities ranging from 1 m/s to 80 m/s was performed, all with employing the calibrated model parameters. The ballistic limit for the TIM assembly is determined as V_{bl}= 34 m/s, such that at the end of this impact event the velocity of the projectile is zero. Below V_{bl} the projectile rebounds and above V_{bl} the target is penetrated. Figure 17 (a) and (b) show the force - displacement responses of the projectile for low and relatively high impact velocities, respectively. The forces increase at the beginning of impact, reach their peaks then decrease with displacement. Similar to the constant velocity loading cases, the reaction force increases with increasing of loading speed, and second peaks developed. While for the same initial loading velocities (Figure 14 and Figure 17(a)), the impact loading results in lower reaction force. For higher impact cases (Figure 17(b)), rebound and penetration can be observed for different impact velocities. Figure 17 also indicates that the TIM absorbs higher amount of impact energy with higher impact velocity.
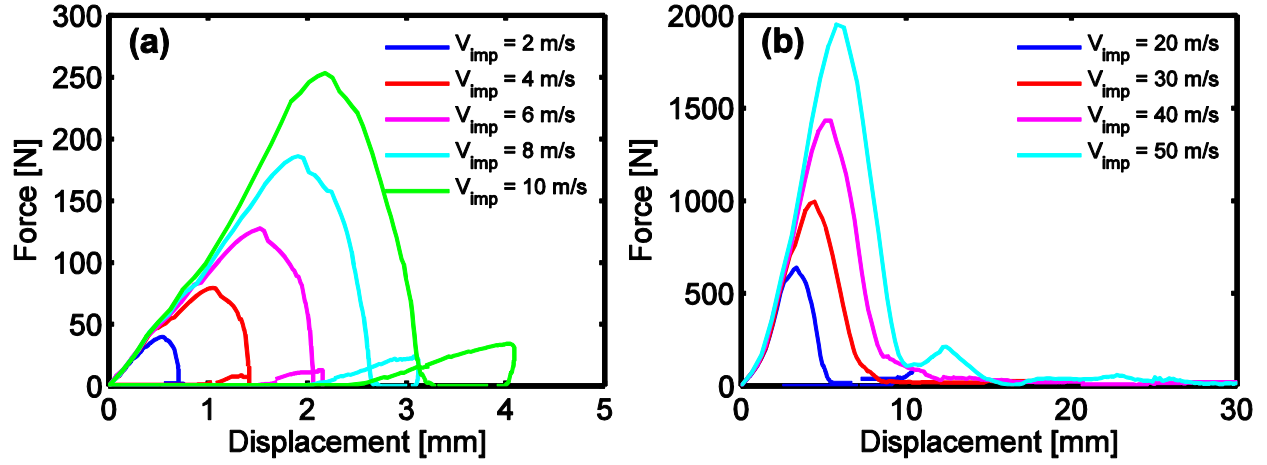
Figure 17. Force - displacement response of projectile with different impact velocities: (a) Low impact velocity, (b) Relatively high velocity.
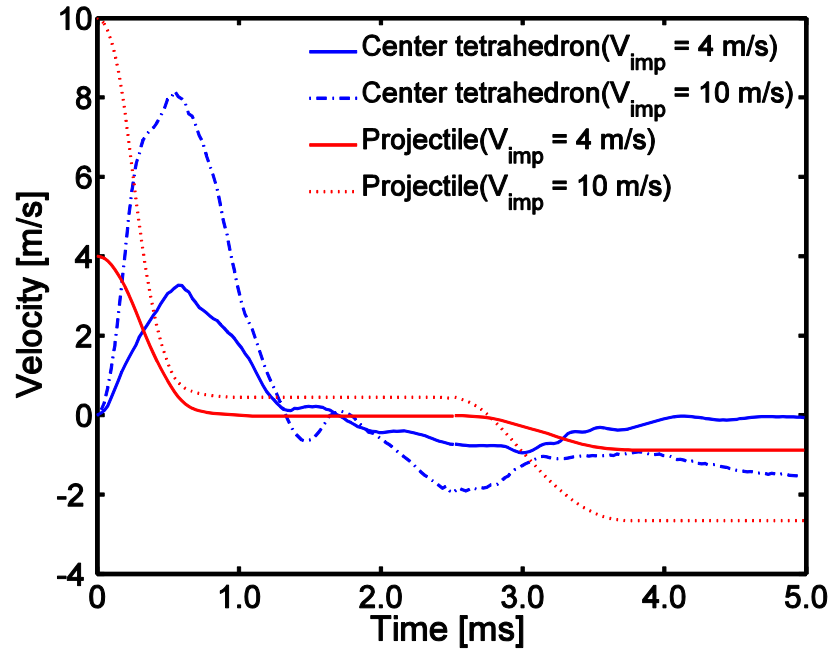

Figure 18. Predicted translational velocities (in load direction) of the center tetrahedron and projectile for loading speeds of V_{imp} = 4 m/s and 10 m/s.

Figure 18 predicts the velocities of center tetrahedron and projectile for impact velocity V_{imp} = 4 and 10 m/s, respectively. Comparison of the results with constant velocity loading (Figure 16) shows that center tetrahedron obtains smaller velocity under impact loading when the initial loading speed for both cases are the same; and after the center tetrahedron decelerated due to interaction with surrounding tetrahedra, the velocity difference between projectile and center tetrahedron is also smaller in the impact loading case, which interprets the differences among force peaks shown in Figure 14 and Figure 17(a).

Figure 19 depicts the velocity histories of the projectile and the center five tetrahedra, Figure

9(c), for four values of the impact velocity V_{imp}. In all cases $V_{imp} \geq V_{bl}$. At the ballistic limit, Figure 19(a), both velocities of the tetrahedra and the projectile reach zero. For impact velocity slightly higher than ballistic limit, V_{imp}= 45 m/s, the velocities of the center tetrahedron and the projectile velocity are only slightly larger than that of the surrounding tetrahedra, Figure 19(b). This indicates that the projectile strongly interacts not only with the center tetrahedron, but due to the topological interlocking, also with the surrounding. For relatively high impact velocity cases shown in Figure 19(c) and (d) this situation changes. In both cases shown, i.e., V_{imp} = 55 and 80 m/s, the center tetrahedron gains much higher velocity than its neighbors. Still, V_{imp} = 55 m/s the projectile velocity is similar to that of the surrounding unit elements, indicating that the TIM assembly continues to provide some level of resistance.   Only at much higher impact velocity, V_{imp} = 80 m/s, is such an interaction lost and the projectile velocity increases beyond that of the surrounding tetrahedra.   The images of the deformed configuration of the TIM assemblies during impact, Figure 20, confirm these different levels of interaction between projectile and the TIM target.
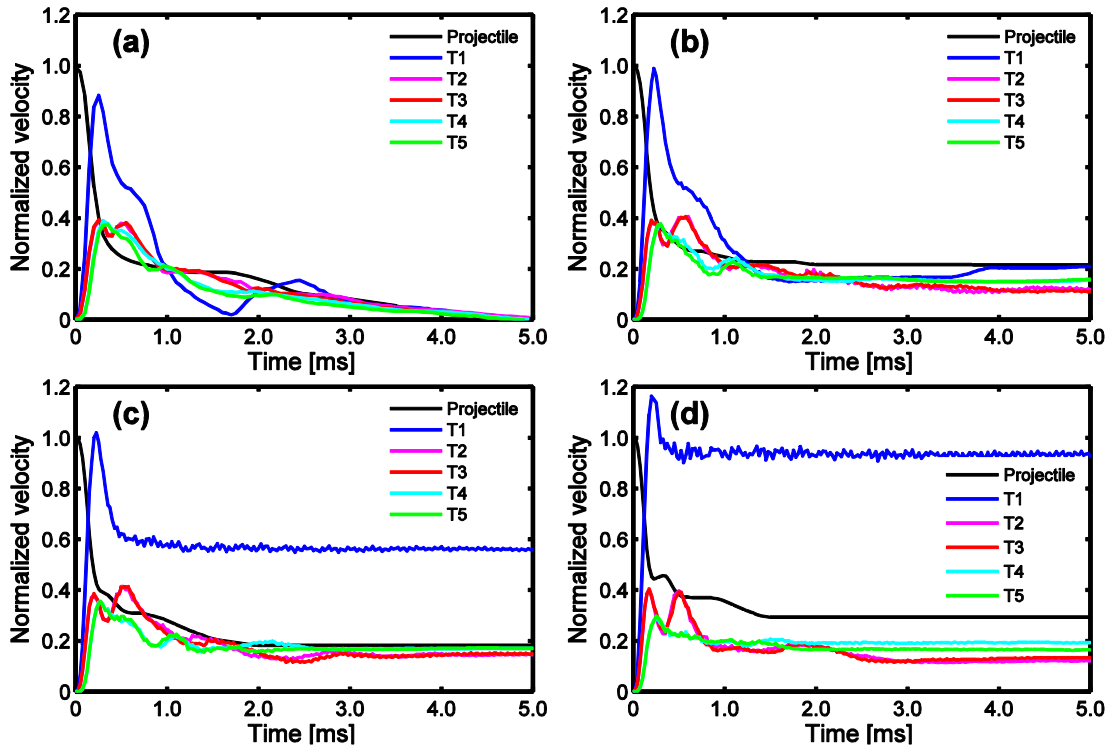

Figure 19. Predicted projectile velocity during impact compared to the velocities of the five central tetrahedra units in the TIM assembly: (a) V_{imp} = 34m/s (b) V_{imp} = 45 m/s (c) V_{imp} = 55 m/s (d) V_{imp} = 80 m/s.
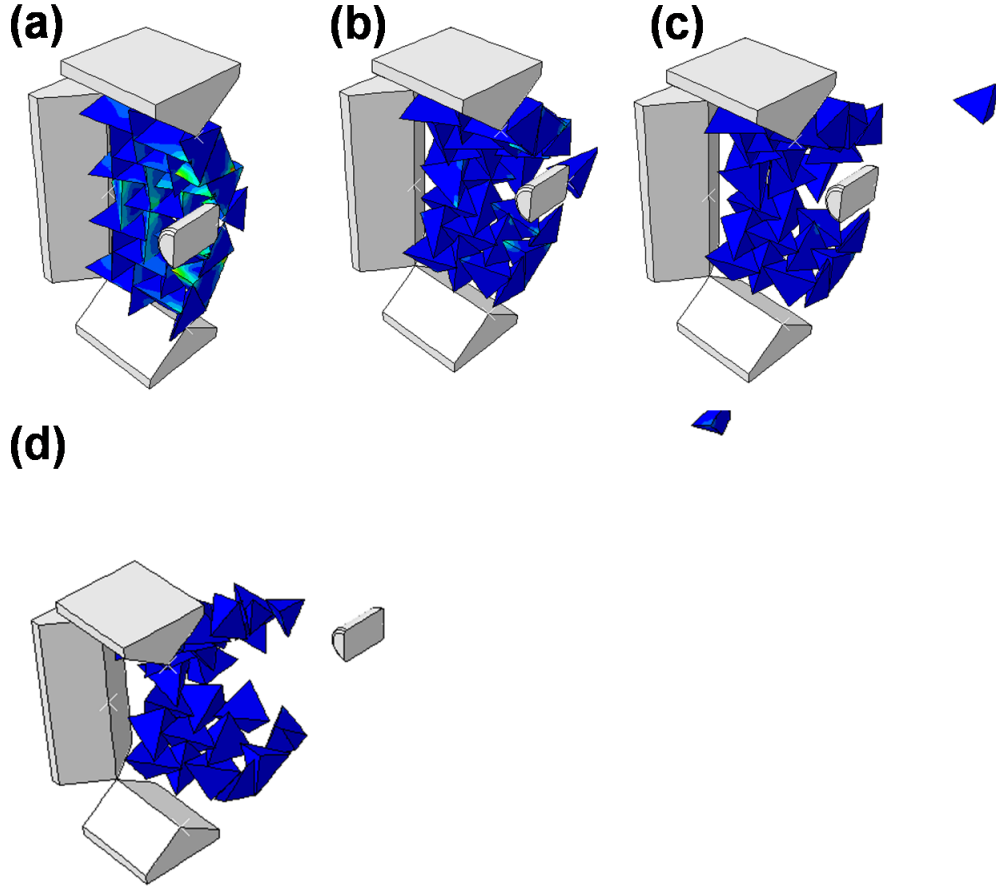
Figure 20. Predicted deformed configurations of the TIM assemblies at time = 5 ms:

(a) V_{imp} = 34 m/s (b) V_{imp} = 45 m/s (c) V_{imp} = 55 m/s (d) V_{imp} = 80 m/s.

The central variable to characterize the resistances of plates and plate-like systems to impact, is the residual velocity of the projectile after passing the target. When the impact velocity is greater than the ballistic limit velocity, the projectile penetrates the target and keeps moving forward with non-zero certain kinetic energy. For conventional metal plates or plate-like targets,

Lambert and Jonas [30] proposed a formula to predict the residual velocity:

$$V_{res} = \begin{cases} 0, & V_{imp} \leq V_{bl} \\ a\left(V_{imp}^{p} - V_{bl}^{p}\right)^{1/p} & V_{imp} > V_{bl} \end{cases} \tag{0}$$

in which a an p are constants to be fitted with the residual velocity data, V_{imp} is impact velocity and V_{bl} is ballistic velocity. Figure 21 depicts the fit to the residual velocity data using the Lambert-Jonas models. A nonlinear least square method was employed to obtain the parameters, which was conducted with `MATLAB` built-in function `lsqnonlin` [36]. The fitted parameters are a = 0.343 and p = 1.487. The coefficient of determination (R^2) is 0.9570, indicating the curve well fits the numerical results.
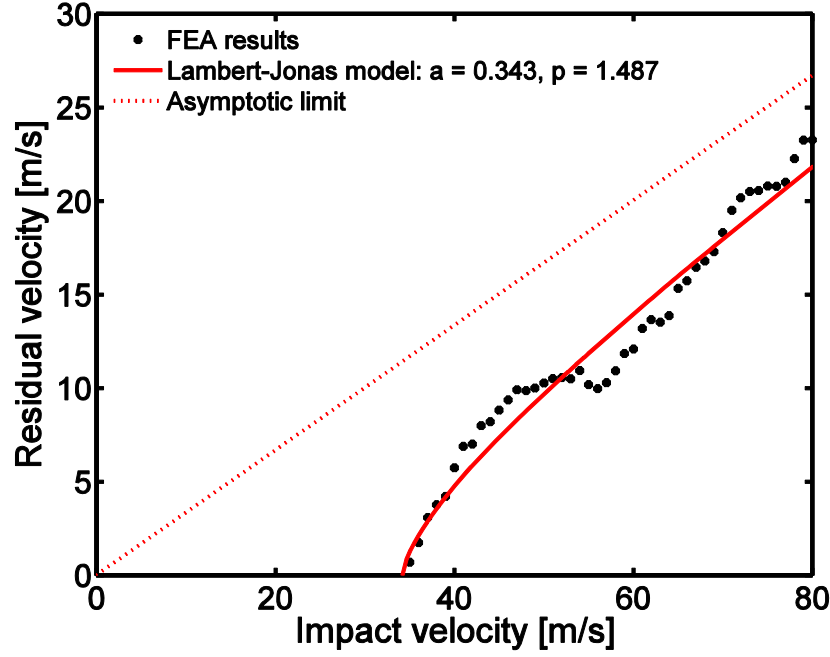
Figure 21. Predicted residual velocities in dependence of the impact velocity and data fit by the Lambert-Jonas model.

The fitted Lambert-Jonas model can provide an overall good description of the numerical results. Still, but for higher impact velocities, the model fits a less accurate than for velocities close to the ballistic limit. A detailed examination of Figure 21 leads to the conclusion that the residual velocities solution can be separated into at least two regimes (below and above 56 m/s). Such differences in the response can be traced back to the velocity history of projectile and tetrahedra, Figure 19, and is due to the differences in interaction with the unit elements in the TIM assembly. In summary, a two limiting conditions can be defined: (i) low velocity regime with strong persisting projectile - target interaction, and (ii) a high velocity regime with weak projectile-target interaction. A transient regime exists at intermediate velocities. The transition regime is of particular interest as a local minimum in the residual velocity is present. In order to capture this response in the Lambert-Jonas formulism, a two-stage expanded Lambert-Jonas model is defined

$$
V_{res} = \begin{cases} 0, & V_{imp} < V_{bl} \\ a_1 \left(V_{imp}^{p_1} - V_{bl}^{p_1} \right)^{1/p_1}, & V_{bl} \leq V_{imp} \leq V_{trans} \\ a_2 \left(V_{imp}^{p_2} - V_V^{p_2} \right)^{1/p_2}, & V_{imp} > V_{bl} \end{cases} \qquad (0)
$$

with V_{trans} the transition velocity between the two limiting regimes, V_V is a virtual ballistic velocity fitted on high impact velocity regime, and a_1, a_2, p_1 and p_2 the characterizing parameters. Figure 22 depicts the residual velocity date fitted to the two-stage model with fit

parameters $a_1 = 0.308$, $a_2 = 0.425$, $p_1 = 1.772$, $p_2 = 1.528$, $V_V = 46$ m/s, and $V_{trans} = 56$ m/s, respectively. The coefficient of determination for low impact velocity is 0.9498 while for high impact velocity is 0.9883, which indicates a much better fitting with two-stage Lambert-Jonas model than the basic model for the high impact velocity regime.

To further explore the finding of the regime with a local minimum in residual velocity, computations were performed with a lower and higher value of μ, 0.15 and 0.25 respectively. Figs.15 and 16 depict the projectile residual velocities, as well as generalized model fits. The fit parameters are shown Table 1. In fitting the parameters, p_1 and p_2 are constrained to be greater than one, as demonstrated in [30]. Comparison of the results in Figs. 14-16 shows that the ballistic velocities and transition velocities increase with a increasing of μ. The charactering parameters a_1, p_2 and V_V increase with μ while a_2 and p_1 decrease monotonically. The two regimes in the residual velocities are present independent of the friction condition, but importance of the transition regime with minimal velocity diminishes or vanishes as the coefficient of friction is increased.
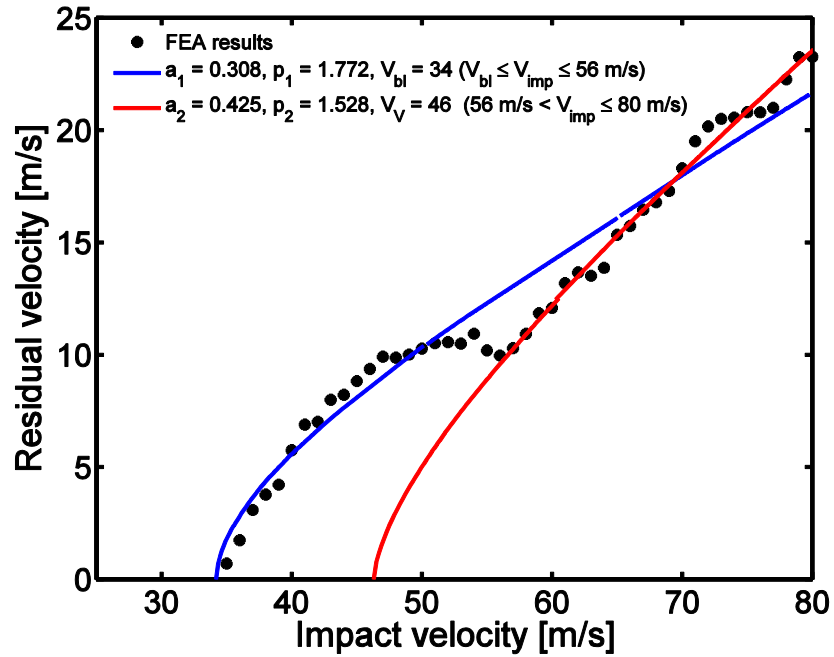

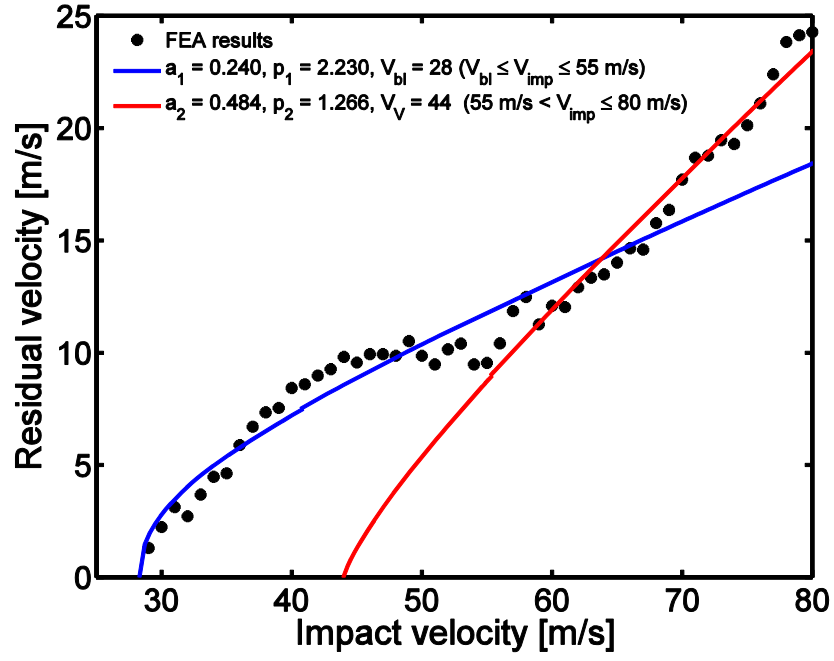Figure 22. Predicted residual velocities and fit by two-stage Lambert-Jonas model ($\mu = 0.20$).

Figure 23. Predicted residual velocities and fit by two-stage Lambert-Jonas model ($\mu = 0.15$).
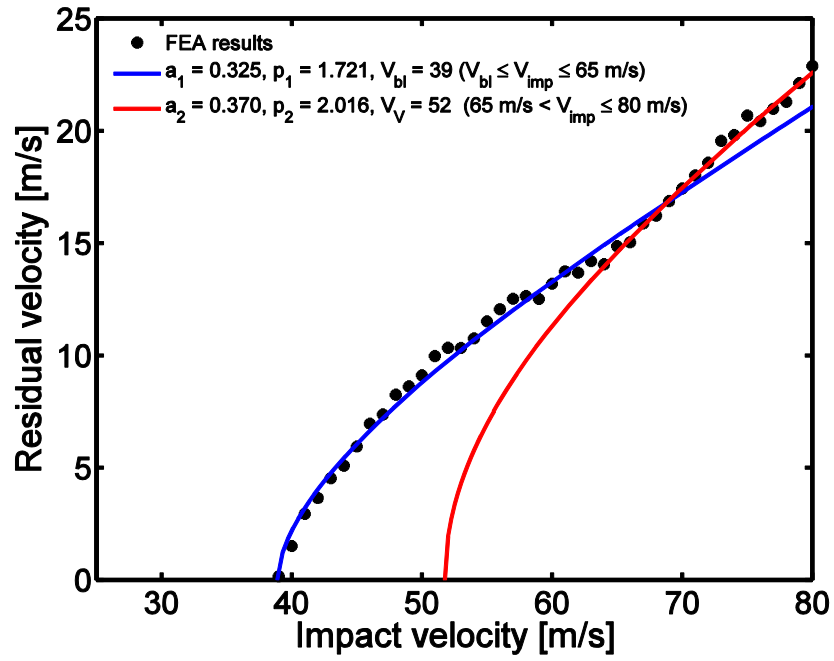

Figure 24. Predicted residual velocities and fit by two-stage Lambert-Jonas model ($\mu = 0.25$).

Table 1. Parameters of the two-stage Lambert-Jonas model

	a_1	a_2	p_1	p_2	V_{bl}[m/s]	V_V[m/s]	V_{trans} [m/s]	R^2
μ= 0.15	0.240	0.484	2.230	1.266	28	44	55	0.9083/0.9592
μ= 0.20	0.308	0.425	1.772	1.528	34	46	56	0.9498/0.9883
μ= 0.25	0.325	0.370	1.721	2.016	39	52	65	0.9914/0.9923

4.3. Fragmentation

Fragmentation commonly occurs for brittle materials subject to impact loading [37-39]. To compare the impact resistance of TIMs made by brittle materials with and without fragmenting, a cohesive zone model (CZM) was further developed. Motivated by the TIM material used in experiments [15], in which the tetrahedra were made with additive manufacturing, the zero thickness cohesive zone (CZ) layers were created parallel to the mid-plane of TIM assembly, i.e., perpendicular to the impact direction, which was meshed with cohesive element `COH3D8`. In each tetrahedron, equally spaced eight CZ layers were inserted. Therefore, each tetrahedron contains 10 solid layers and 8 CZ layers (Fig. 4). A bilinear traction-separation law was used to describe the constitutive response of CZM, with maximum strength σ_{max}= E/100, failure separation δ_f=s_0/1000 and damage initiation separation δ_0= δ_F/10. Since `ABAQUS/Explicit` method is used to solve the dynamic problem, the density of the CZ layer needs to be defined. In the simulations for TIMs with CZ layers, the density of the CZ layer is ρ_{coh} = 1.0 kg/m^3 which does not increase the inertia of the structure significantly, as well as the computational difficulty [34]. Aside from of the CZ properties, all the other properties and conditions are the same with that used in the impacting simulations of TIMs with isotropic tetrahedra.

Four impact velocity cases (V_{imp} = 34, 45, 55 and 80 m/s) were performed with the model enhanced by cohesive zone elements. Table 2 lists the terminal velocities for isotropic TIM and CZ enhanced TIM models. Figure 25 compares the projectile velocities with V_{imp}=55 m/s, and similar comparison can be obtained for other impact velocity cases and Figure 26 shows the fragmentation of CZ enhanced TIMs for different impact velocities. The results show that the CZ enhanced model resists impact better with lower projectile residual velocity, but the difference is not significant when impact velocity is high.

Table 2. Terminal velocities of TIMs with and without CZ enhancement [m/s]

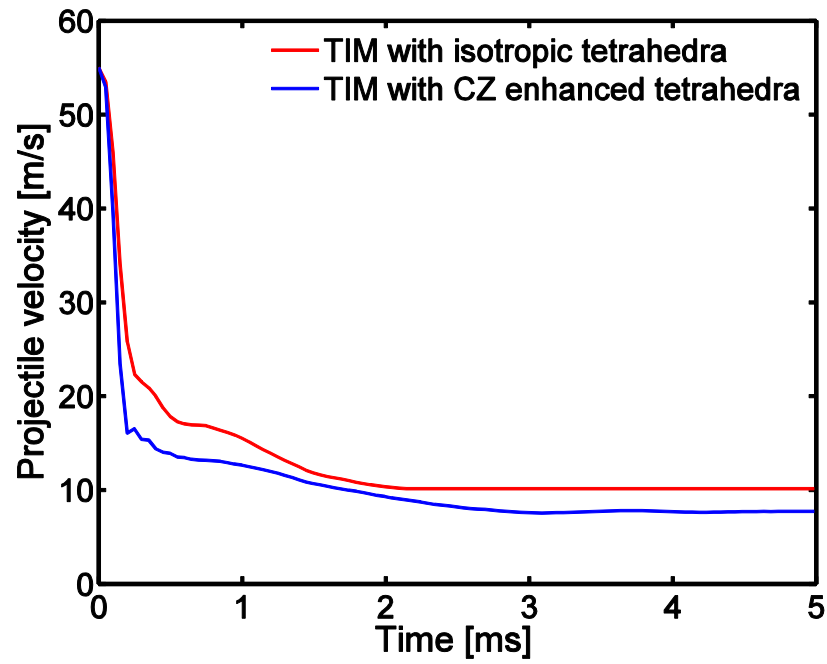|	V_{imp}=34 m/s	V_{imp}= 45 m/s	V_{imp}=55 m/s	V_{imp}= 80 m/s
Isotropic TIM	0	8	10	23
CZ enhanced TIM	-2	2	8	18

Figure 25. Projectile velocity for isotropic and CZ enhanced TIM models (V_{imp}= 55 m/s).
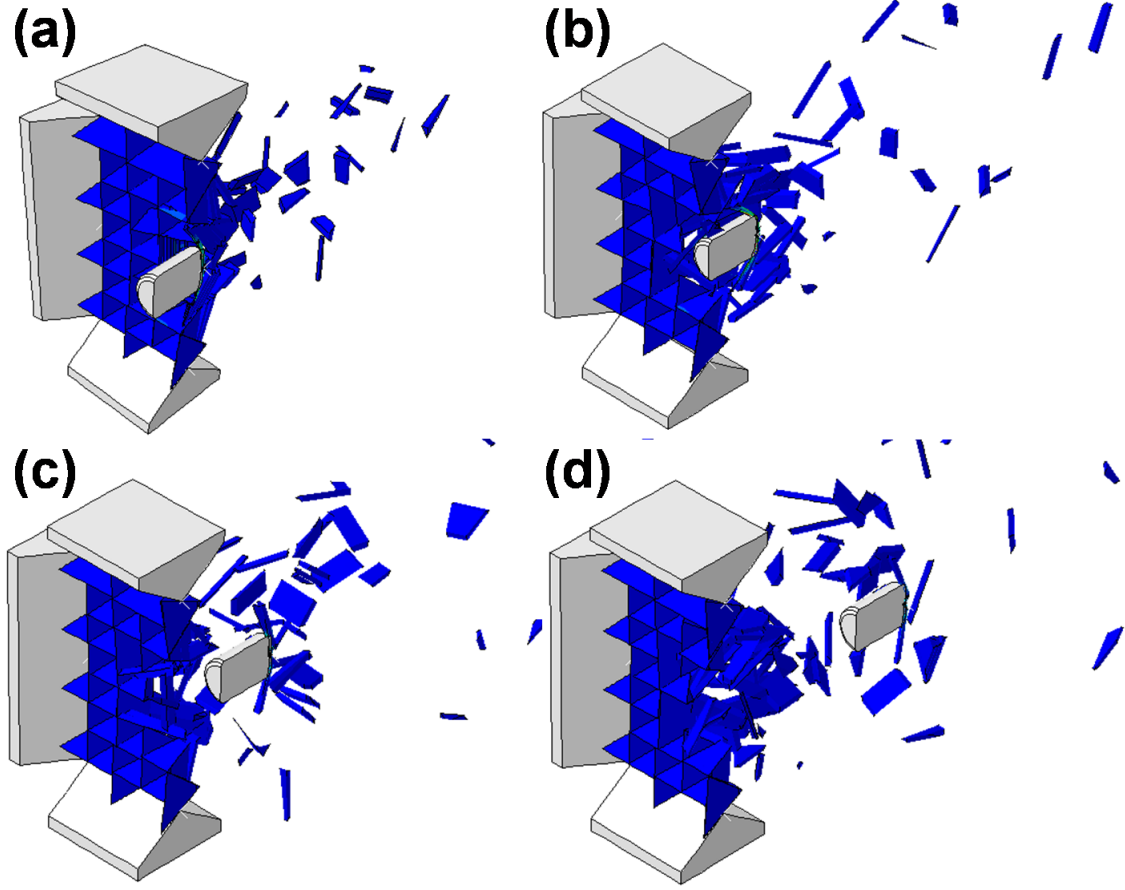
Figure 26. Fragmentation of CZ enhanced TIMs at time 5 ms: (a) V_{imp} = 34 m/s (b) V_{imp} = 45 m/s (c) V_{imp} = 55 m/s (d) V_{imp} = 80 m/s.

We furthermore explore the multiscale characteristics of the failure response of TIMs by expanding the considerations on the cohesive zone model approach to failure in the context of TIMs. In addition to the parameter set considered for the results shown in the initial part of this section, a range of computations was conducted in which the cohesive zone model parameters were altered systematically. Table 3 summarizes the failure parameters. In the model series the internal material length scale and the material strength are altered, still the material stiffness and the failure energy are kept constant. Such a series of computations allows for the study of the influence of the internal material length scale on the failure behavior. Figure 27 depicts the predicted residual velocities of the impactor (initial velocity V_{imp} = 80 m/s) after interaction with the target.

Table 3: Cohesive Zone Model parameters

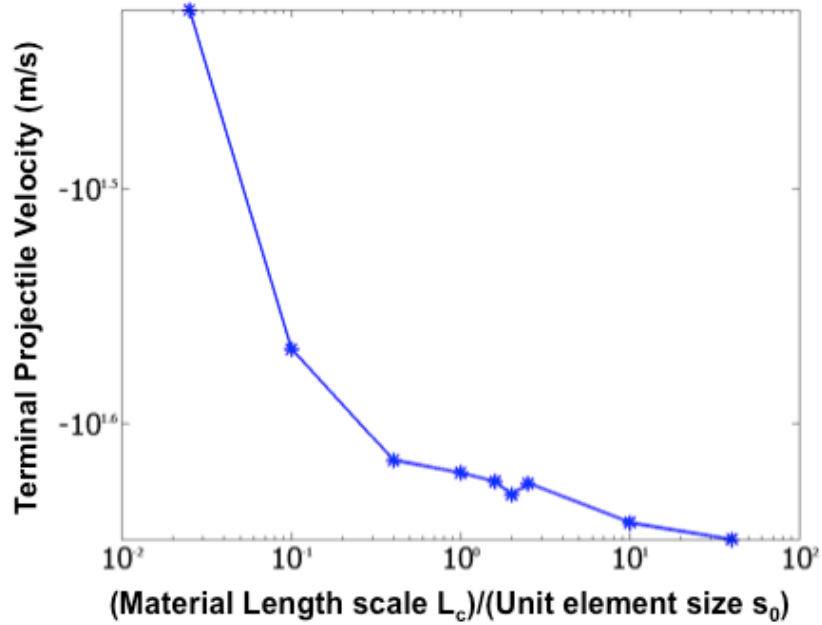| Test #	σ_{max}	δ_f	L_c/s_0	CZ Energy
1	$E/50$	$s_0/2000$	0.025	$s_0 E/100000$
2	$E/100$	$s_0/1000$	0.1	$s_0 E/100000$
3	$E/200$	$s_0/500$	0.4	$s_0 E/100000$
4	$E/316.2$	$s_0/316.2$	1	$s_0 E/100000$
5	$E/400$	$s_0/250$	1.6	$s_0 E/100000$
6	$E/447.2$	$s_0/223.614$	2	$s_0 E/100000$
7	$E/500$	$s_0/200$	2.5	$s_0 E/100000$
8	$E/1000$	$s_0/100$	10	$s_0 E/100000$
9	$E/2000$	$s_0/50$	40	$s_0 E/100000$

Figure 27: Predicted residual velocity of the penetrator in dependence of the material failure characteristic length scale.

The results of Fig. 27 indicate a size effect on the residual velocity in dependence of the material characteristic length scale. For cases where the material length scale is large compared to the size of the unit tetrahedron, the residual velocity was found to be nearly constant and independent of the material length scale.

5. Discussion

The simulations of the TIM response under constant loading speed, Figure 14 to 16, provide insight into the relevance of the material parameters in the TIM system. The responses can be divided into three categories according to loading speeds: quasi-static response at low speeds, combination of quasi-static and dynamic response, and dominant dynamic. For quasi-static case, a quasi-ductile response can be observed, which agrees with the experimental observation [15]. For moderate indentation speeds, the force-deflection response can be considered as the combination of quasi-static response and unconfined TIM under same indention speed. As shown in Appendix, the transition speed is determined by the density of TIM material, the normal contact behavior, while coefficient of friction does not affect the inertia responses significantly.

The dynamic characteristics of TIM are further investigated with projectile impact loading conditions. The projectile residual velocity is used as the parameter to illustrate TIM's resistibility to impact, with Lambert-Jonas models being employed to describe the numerical results. To have a more accurate description of the residual velocity results, an extended two-stage Lambert-Jonas model is developed. For conventional plate, Børvik et al. [40] fitted the Lambert-Jonas formula with $a = 0.76$ and $p = 2.36$ based on experimental data for ballistic penetration of steel plates. Chi et al. [41] applied the model to a bi-layer metal system and obtained ranges of the parameters for different thicknesses of metal plates: $0.93 < a < 0.97$ and $1.72 < p < 2.14$. Other experimental and numerical results [42-49] also indicate that for homogeneous plates and composite plates, a is close to 1.0 and p is close to 2.0. Comparing to the parameters in the Lambert-Jonas model for TIM with conventional plates, the parameter p is close to that for conventional plates while a is significantly smaller. According to Lambert-Jonas formulism, a smaller a indicates lower residual velocity, therefore, more kinetic energy absorption.

Residual velocity comparison was performed between TIMs with isotropic tetrahedra or CZ enhanced tetrahedra. When the impact velocity is close to ballistic velocity of TIM with isotropic tetrahedra, the residual velocities for TIM with CZ layers are smaller. The increasing of TIM stiffness is due to the fragmentation. At the end of impact events, energy distribution of the entire system show that, the kinetic energy of the tetrahedra and fragments

of TIMs with CZ layers is higher than TIMs with isotropic tetrahedra. These results can be confirmed with the result shown in Figure 26. For example, when the impact velocity is 34 m/s, every tetrahedron is almost motionless for TIMs without CZ layers (Figure 20(a)) at the end of impact; while for TIMs with CZ layers (Figure 26(a)), fragments fly with certain kinetic energy. Therefore, because of fragmentation, the implementation of CZ layers into TIM actually increases TIM's dynamic stiffness. The increment in dynamic stiffness is remarkable when impact velocities are close to ballistic velocity. For high impact velocities (V_{imp} = 55 and 80 m/s), the difference of kinetic energies of tetrahedra/fragments for both models is not significant, resulting in similar residual velocities as shown in Table. 2. Figure 26 also illustrates that damage can be localized for TIMs: only the tetrahedra directly impacted and their neighbors are damaged, while the tetrahedra away from the impact center keep their integrities. A critical internal length scale appears to exist. For smaller internal material length scales that those of the critical dimension, the residual velocity is found to be dependent on the material length scale and is predicted to increase with a decrease in material length scale. This finding appears to parallel the size effects found in quasi-brittle structures as widely discussed in the structural mechanics literature.

6.   Conclusions

The present work numerically investigated the dynamic responses of TIM under constant velocity and projectile impact loading with finite element method. The FEA model is calibrated with published experimental data. The resistances of TIM under constant velocity and projectile impact were examined. Numerical results indicate that: (i) TIM responses to constant velocity loading can be categorized into three groups according to the indention speeds: quasi-static response, combination of dynamic and quasi-static response, and pure dynamic response. At low velocities, the response of TIMs emerges as the sum of the inertia (unconfined TIM) and the quasi-static response. For higher velocity cases, the indenter imparts multiple inertia responses. (ii)The terminal velocities of projectile for impact velocities form 1 m/s to 80 m/s are obtained, Investigation of the residual velocities of projectile after penetrating shows TIMs follow two-stage generalized analytical models. The parameters in extended Lambert-Jonas models for TIM are fitted on obtained numerical results, with parameter p is close to conventional solid metallic plates for high velocity regime but is smaller for low velocity regime, while parameter a is much smaller for both stages.   For given p in Lambert-Jonas formulism, a smaller a indicates lower residual velocity, hence higher kinetic energy absorption. (iii) Comparison between TIMs with and without CZ layers show that TIMs with CZ layers can resist projectile better when the impact

velocity is close to ballistic velocity. When the impact velocity is higher, the difference of the two TIM models in resisting impact is not significant. Here we demonstrate a size effect on failure for the topologically interlocked materials and provide a path such that these material systems could be exploited to create impact resistant systems.

7.   Collaboration

During the project period the PI has conducted extensive coordination and communication with research staff at ARL, E. Habtour and J. Riddick. The PI has provided ARL staff the Python scripting code, stl files for 3D printing of TIM assemblies in house at ARL, and has delivered input files for ABAQUS computations to ARL. The PI visited ARL on Sep. 26, 2013 and presented a seminar talk summarizing the results of this work.

8.   Publications

The following publications have resulted from this effort:

Journal Publications
Y.-Z. Feng, E. Habtour, J. Riddick, T. Siegmund, "Impact mechanics of topologically interlocked materials," International Journal of Impact Engineering, to be submitted.

ARL-Reports
Y.-Z. Feng, T. Siegmund, "Python scripting in ABAQUS to create finite element models and 3D print physical models for granular crystals," submitted to ARL as Technical Report.

Conferences Presentations:
Y.-Z. Feng, E. Habtour, J. Riddick, T. Siegmund, "Damage analysis of a hybrid energy absorption layer based on the principle of topologically interlocking materials," Proceedings of the 2013 International Mechanical Engineering Congress and Exposition, The American Society of Mechanical Engineers. San Diego, CA, Nov. 2013; paper IMECE2013-66426.
Y.-Z. Feng, T. Siegmund, "Dynamic and failure analysis of topologically interlocked materials subjected to impact," EMI-2013, 2013 Engineering Mechanics Institute Conference of ASCE, August 4-7, 2013, Northwestern University, Evanston, IL, USA, Abstract #371.

References

[1] M.F. Ashby, Y.J.M. Brechet, Designing hybrid materials, Acta Materialia, 51 (2003) 5801-5821.

[2] M.F. Ashby, Hybrids to fill holes in material property space, Philosophical Magazine, 85 (2005) 3235-3257.

[3] M. Ashby, Hybrid Materials to Expand the Boundaries of Material-Property Space, Journal of the American Ceramic Society, 94 (2011) s3-s14.

[4] A.Y. Dyskin, Y. Estrin, A.J. Kanel-Belov, E. Pasternak, Topological interlocking of platonic solids: a way to new materials and structures, Philosophical Magazine Letters, 83 (2003) 197-203.

[5] A.V. Dyskin, Y. Estrin, A.J. Kanel-Belov, E. Pasternak, Interlocking properties of buckyballs, Physics Letters A, 319 (2003) 373-378.

[6] Y. Estrin, A.V. Dyskin, E. Pasternak, Topological interlocking as a material design concept, Materials Science & Engineering C-Materials for Biological Applications, 31 (2011) 1189-1194.

[7] A.V. Dyskin, Y. Estrin, E. Pasternak, H.C. Khor, A.J. Kanel-Belov, The principle of topological interlocking in extraterrestrial construction, Acta Astronautica, 57 (2005) 10-21.

[8] M. Glickman, The G-block system of vertically interlocking paving, in: Proceeding of the second international conference on concrete block paving, Delft, 1984, pp. 345.

[9] A.V. Dyskin, Y. Estrin, A.J. Kanel-Belov, E. Pasternak, A new principle in design of composite materials: reinforcement by interlocked elements, Composites Science and Technology, 63 (2003) 483-491.

[10] A.V. Dyskin, Y. Estrin, A.J. Kanel-Belov, E. Pasternak, A new concept in design of materials and structures: Assemblies of interlocked tetrahedron-shaped elements, Scripta Materialia, 44 (2001) 2689-2694.

[11] Y. Estrin, A.V. Dyskin, E. Pasternak, S. Schaare, S. Stanchits, A.J. Kanel-Belov, Negative stiffness of a layer with topologically interlocked elements, Scripta Materialia, 50 (2004) 291-294.

[12] S. Schaare, A.V. Dyskin, Y. Estrin, S. Arndt, E. Pasternak, A. Kanel-Belov, Point loading of assemblies of interlocked cube-shaped elements, International Journal of Engineering Science, 46 (2008) 1228-1238.

[13] C. Brugger, Y. Brechet, M. Fivel, Experiments and numerical simulations of interlocked materials, in: A.K.T. Lau, J. Lu, V.K. Varadan, F.K. Chang, J.P. Tu, P.M. Lam (Eds.) Multi-Functional Materials and Structures, Pts 1 and 2, 2008, pp. 125-128.

[14] A.V. Dyskin, Y. Estrin, A.J. Kanel-Belov, E. Pasternak, Toughening by fragmentation - How topology helps, Advanced Engineering Materials, 3 (2001) 885-888.

[15] S. Khandelwal, T. Siegmund, R.J. Cipra, J.S. Bolton, Transverse loading of cellular topologically interlocked materials, International Journal of Solids and Structures, 49 (2012) 2394-2403.

[16] A. Mather, R. Cipra, T. Siegmund, Structural integrity during remanufacture of a topologically interlocked material, International Journal of Structural Integrity, 3 (2012) 61-78.

[17] Y. Estrin, A.V. Dyskin, E. Pasternak, H.C.K. Khor, A.J. Kanel-Belov, Topological interlocking of protective tiles for the space shuttle, Philosophical Magazine Letters, 83 (2003) 351-355.

[18] M. Carlesso, R. Giacomelli, T. Krause, A. Molotnikov, D. Koch, S. Kroll, K. Tushtev, Y. Estrin, K. Rezwan, Improvement of sound absorption and flexural compliance of porous alumina-mullite ceramics by engineering the microstructure and segmentation into topologically interlocked blocks, Journal of the European Ceramic Society, 33 (2013) 2549-2558.

[19] M.O.W. Richardson, M.J. Wisheart, Review of low-velocity impact properties of composite materials, Composites Part A: Applied Science and Manufacturing, 27 (1996) 1123-1131.

[20] S. Abrate, Impact on composite structures, Cambridge university press, 2005.

[21] G. Ben-Dor, A. Dubinsky, T. Elperin, Ballistic Impact: Recent Advances in Analytical Modeling of Plate Penetration Dynamics–A Review, Applied Mechanics Reviews, 58 (2005) 355-371.

[22] F. Zhu, G. Lu, A review of blast and impact of metallic and sandwich structures, EJSE Special Issue: Loading on Structures, (2007) 92-101.

[23] W. Goldsmith, J.L. Sackman, An experimental study of energy absorption in impact on sandwich plates, International Journal of Impact Engineering, 12 (1992) 241-262.

[24] H.-Y.T. Wu, C. Fu-Kuo, Transient dynamic analysis of laminated composite plates subjected to transverse impact, Computers & Structures, 31 (1989) 453-466.

[25] Y. Duan, M. Keefe, T.A. Bogetti, B.A. Cheeseman, B. Powers, A numerical investigation of the influence of friction on energy absorption by a high-strength fabric subjected to ballistic impact, International Journal of Impact Engineering, 32 (2006) 1299-1312.

[26] B.C. Simonsen, L.P. Lauridsen, Energy absorption and ductile failure in metal sheets under lateral indentation by a sphere, International Journal of Impact Engineering, 24 (2000) 1017-1039.

[27] J. Dean, C.S. Dunleavy, P.M. Brown, T.W. Clyne, Energy absorption during projectile perforation of thin steel plates and the kinetic energy of ejected fragments, International Journal of Impact Engineering, 36 (2009) 1250-1258.

[28] H.N.G. Wadley, M.R. O'Masta, K.P. Dharmasena, B.G. Compton, E.A. Gamble, F.W. Zok, Effect of core topology on projectile penetration in hybrid aluminum/alumina sandwich structures, International Journal of Impact Engineering, 62 (2013) 99-113.

[29] R.F. Recht, T.W. Ipson, Ballistic Perforation Dynamics, Journal of Applied Mechanics, 30 (1963) 384-390.

[30] J.P. Lambert, G.H. Jonas, Towards standardization in terminal ballistics testing: velocity representation, in, USA Ballistic Research Laboratories, Aberdyn, Maryland, USA, 1976.

[31] J.H. Conway, S. Torquato, Packing, Tiling, and Covering with Tetrahedra, Proceedings of the National Academy of Sciences of the United States of America, 103 (2006) 10612-10617.

[32] G.I. Barenblatt, The mathematical theory of equilibrium cracks in brittle fracture, in: Advances in Applied Mechanics, Academic Press, New York, 1962, pp. 55-129.

[33] N. Moës, J. Dolbow, T. Belytschko, A finite element method for crack growth without remeshing, International Journal for Numerical Methods in Engineering, 46 (1999) 131-150.

[34] K. Song, C.G. Dávila, C.A. Rose, Guidelines and parameter selection for the simulation of progressive delamination, in: abaqus User's Conference, Newport, Rhode Island (Hibbit Karlsson and Sorensen, USA, 2008), 2008, pp. 1-15.

[35] Dassault Systèmes, Abaqus user manual, 2012.

[36] Matlab 2013a, The MathWorks Inc. 2013.

[37] G.T. Camacho, M. Ortiz, Computational modelling of impact damage in brittle materials, International Journal of Solids and Structures, 33 (1996) 2899-2938.

[38] C. Denoual, F. Hild, Dynamic fragmentation of brittle solids: a multi-scale model, European Journal of Mechanics - A/Solids, 21 (2002) 105-120.

[39] D.E. Grady, Local inertial effects in dynamic fragmentation, Journal of Applied Physics, 53 (1982) 322-325.

[40] T. Børvik, M. Langseth, O.S. Hopperstad, K.A. Malo, Ballistic penetration of steel plates, International Journal of Impact Engineering, 22 (1999) 855-886.

[41] R. Chi, A. Serjouei, I. Sridhar, G.E.B. Tan, Ballistic impact on bi-layer alumina/aluminium armor: A semi-analytical approach, International Journal of Impact Engineering, 52 (2013) 37-46.

[42] A. Seyed Yaghoubi, B. Liaw, Thickness influence on ballistic impact behaviors of GLARE 5 fiber-metal laminated beams: Experimental and numerical studies, Composite Structures, 94 (2012) 2585-2598.

[43] S. Dey, T. Børvik, X. Teng, T. Wierzbicki, O.S. Hopperstad, On the ballistic resistance of double-layered steel plates: An experimental and numerical investigation, International Journal of Solids and Structures, 44 (2007) 6701-6723.

[44] T. Børvik, S. Dey, A.H. Clausen, Perforation resistance of five different high-strength steel plates subjected to small-arms projectiles, International Journal of Impact Engineering, 36 (2009) 948-964.

[45] G. Ben-Dor, A. Dubinsky, T. Elperin, A model of high speed penetration into ductile targets, Theoretical and Applied Fracture Mechanics, 28 (1998) 237-239.

[46] S.T. Mileiko, O.A. Sarkisyan, Phenomenological model of punch-through, Journal of Applied Mechanics and Technical Physics, 22 (1981) 711-713.

[47] F. Larsson, Damage tolerance of a stitched carbon/epoxy laminate, Composites Part A: Applied Science and Manufacturing, 28 (1997) 923-934.

[48] S.K. García-Castillo, S. Sánchez-Sáez, E. Barbero, Behaviour of uniaxially preloaded aluminium plates subjected to high-velocity impact, Mechanics Research Communications, 38 (2011) 404-407.

[49] L. Xue, W. Mock Jr, T. Belytschko, Penetration of DH-36 steel plates with and without polyurea coating, Mechanics of Materials, 42 (2010) 981-1003.

Appendix. Determination of the TIM Inertia

To investigate the determination of the 'inertia' of TIMs, unconfined TIM models were employed for different tetrahedron material densities, COFs and contact stiffness. Loading speed is $V_0 = 4$ m/s for all the unconfined cases. Figure A-1 shows the predicted peak forces for different material densities. The material densities are normalized with the density of engineering ABS ($\rho_0 = 950$ kg/m^3). Approximate linear dependency of peaks with the density can be observed from Figure A-1. When $\rho = 0.05\rho_0$, the peak of the reaction forces is about 20 N, while when $\rho = 2.0\rho_0$, the peak of the reaction forces is about 177 N. Figure A-2 shows the predicted peak forces for normalized COFs range from 0.05 to 2.0. The COFs are normalized with calibrated COF ($\mu_0 = 0.2$). With 40 times increase (2/0.05) in COF, the peak value increases only about 33%. Figure A-3 depicts the predicted peak forces for different contact stiffness. The contact stiffness is normalized with calibrated value ($K^*_0 = 0.38$). The peak force is about 39 N when $K^* = 0.05K^*_0$, and reaches 154 N when $K^* = 2.0K^*_0$, a total 4 time increase over the range of contact stiffness from $0.05K^*_0$ to $2.0K^*_0$.
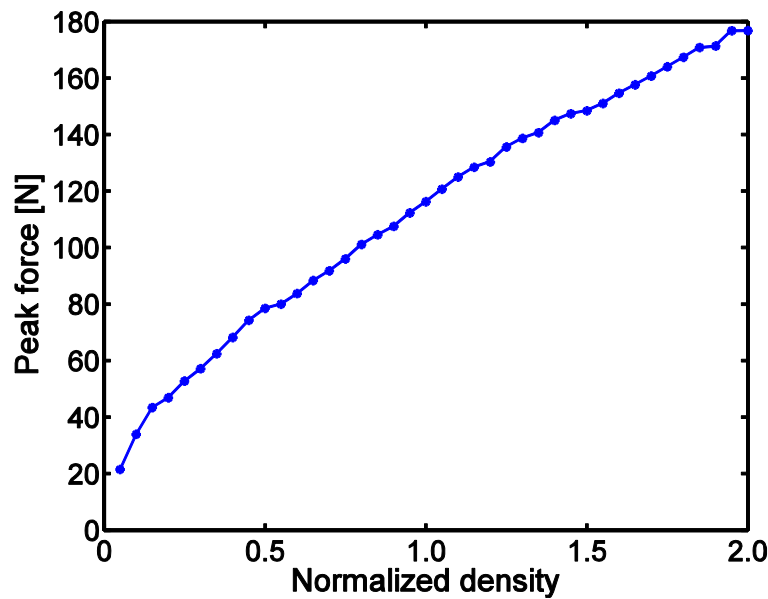

Figure A-1. Predicted peak reaction forces of unconfined TIM for various values material densities.
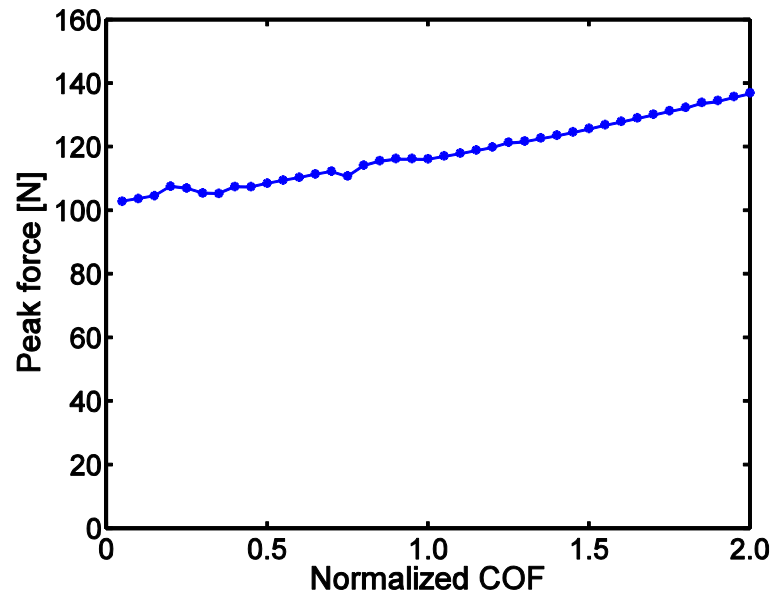
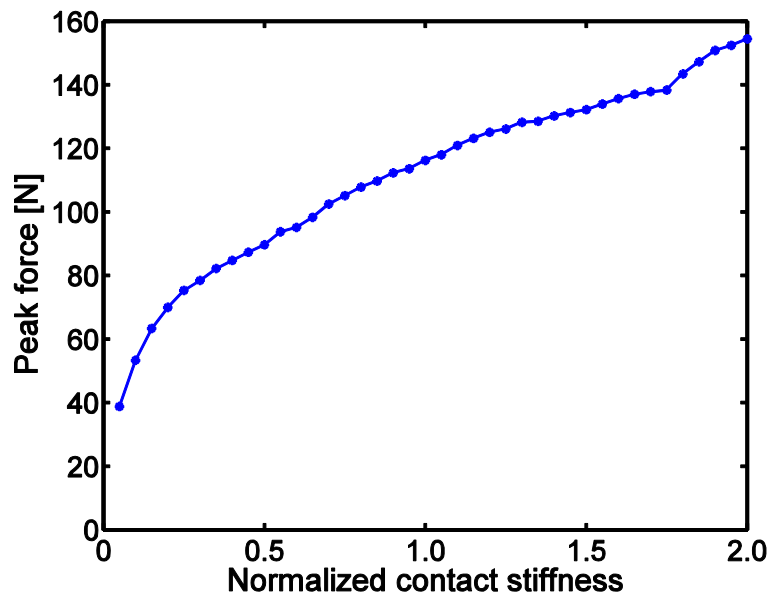Figure A-2. Predicted peak reaction forces of unconfined TIM for various values of coefficients of friction.

Figure A-3. Predicted peak reaction forces of unconfined TIM for various contact stiffness.

List of Symbols and Abbreviations

a: Parameter in Lambert-Jonas model

a_1, a_2: Parameters in extended Lambert-Jonas models

c_d: Dilatational wave speed

D: Projectile diameter

E: Young's modulus of tetrahedron material

H_{drop}: Drop height in drop tower testing

K: Contact stiffness

K^*: Normalizedcontact stiffness

L: Mid-plane dimension of topologically interlocked material assembly

m_0: Mass of a single tetrahedron

M: Projectile mass

M_{drop}: Drop mass in drop tower testing

N: Number of tetrahedra in one row/column of topologically interlocked material assembly

p: Parameters in Lambert-Jonas models

p_1 and p_2: Parameters in extended two-stage Lambert-Jonas models

s_0: Edge length of regular tetrahedron

t: Thickness of topologically interlocked material assembly

V_0: Constant velocity

V_{bl}: Ballistic velocity

V_{imp}: Impact velocity

V_{res}: Residual velocity

V_V: Fitted virtual ballistic velocity of TIM

δ_0, δ_f: Damage initiation separation and failure separation in CZM

ν: Poison's ratio of tetrahedron material

μ: Coefficient of friction

$\rho_0, \hat{\rho}$: Densities of tetrahedron and projectile respectively

ρ_{coh}: Density of cohesive layers

σ_{max}: Maximum strength of CZM

COF: Coefficient of friction

CZ, CZM: Cohesive zone and cohesive zone model

TIM: Topologically interlocked material